広島大学学位請求論文

Search for sub-eV scalar and pseudoscalar fields via four-wave mixing with tabletop lasers

(テーブルトップレーザーを用いた四光波混合によるsub-eVスカラー・擬スカラー場の探索)

2016年

広島大学大学院理学研究科
物理科学専攻

長谷部　孝

目次

Search for sub-eV scalar and pseudoscalar fields via four-wave mixing with tabletop lasers

Takashi Hasebe

Department of Physics Science,
Graduate School of Science
Hiroshima University
2016

Abstract

More than 90% of the energy density in the universe is supposed to be occupied by dark matter and dark energy. Hypothetical low mass neutral bosons can be the candidates for such dark components.

For example, the low mass scalar field called dilaton is predicted above neV mass scale as the candidate for origin of dark energy. It predicted by the scalar-tensor theory with Λ (STTΛ) which is one of the alternative gravitational theories. The pseudoscalar field, axion predicted by the quantum chromodynamics (QCD) below sub-eV mass region can be one of the reasonable candidates for cold dark matter. These scalar and pseudoscalar fields may couple to photons via extremely weak interactions. Therefore, search for low mass scalar and pseudoscalar fields with extremely high intensity laser fields has been proposed.

Quasi parallel colliding system (QPS) is a system to produce resonance states of low mass scalar and pseudoscalar fields via photon scatterings in a focusing laser. By focusing two-color lasers on the same optical axis, the frequency-shifted photon is emitted from the focal volume as the signature of the resonance production. This phenomenon is regarded as the four-wave mixing process in vacuum.

In this thesis, a search for scalar and psudoscalar fields via QPS was performed by combining a 9.3 μJ/0.9 ps Ti-Sapphire laser and 100 μJ/9 ns Nd:YAG laser at 2.3×10^{-2} Pa. As a result, no significant signal was observed and the exclusion limits for scalar and psudoscalar fields were obtained below 0.15 eV mass range.

Furthermore, the four-wave mixing process occurring in atoms was observed at an atmospheric pressure. The pressure dependence of the four-wave mixing photons emitted from residual gas in the vacuum chamber were measured. The number of them were negligible at 2.3×10^{-2} Pa.

The experimental methods established in this thesis can be basically applicable to higher intensity laser experiments.

Contents

List of Figures

List of Tables

1 Introduction

1.1 Physics Motivation

Ordinary matter composed of quarks and leptons occupies only 5% of the energy density of our universe. Unknown components called dark energy and dark matter occupy the remaining density. This indicates that modifications of standard theories of cosmology and elementary particle physics are required for describing the true nature of the universe. Therefore, uncovering dark energy and dark matter is one of the most crucial subjects in modern physics.

The existence of dark matter is strongly indicated by a number of astronomical observations. Some reasonable candidates for dark matter are predicted by theories beyond the standard model in particle physics. On the other hand, the mechanism for creating dark energy has not been understood yet. A number of dark energy models have been suggested. However, there is no experimental result strongly supports a specific dark energy model.

Hypothetical low mass neutral bosons can be candidates for these dark components. For example, a scalar type boson called dilaton is predicted above neV mass scale by one of the alternative gravitational theory. Dilaton can be the candidate for the origin of dark energy. Furthermore, a pseudoscalar type boson called axion is predicted below meV mass range by the quantum chromodynamics (QCD) as the reasonable candidate for cold dark matter. Both dilaton and axion are interpreted as Numbu-Goldstone (NB) bosons [1, 2] as a result of spontaneous symmetry breakings occurred in the early universe. Therefore they supposed to be have extremely light masses. They also interact with matter fields very weakly. If these bosons interact with electromagnetic fields, even if only slightly, they can be proved by pumping enormous amount of coherent photons to a local space in the vacuum.

1.2 Dark energy models with scalar fields

The accelerating universe was discovered by observations of redshifts of type Ia supernova[3, 4, 5]. It is supposed that unknown energy called dark energy expands the universe. In modern cosmology, the cosmological constant Λ is interpret as the origin of dark energy.

Based on the assumption that Λ is the vacuum energy at the energy scale of the quantum gravity field, the theoretical value of Λ is estimated as $\Lambda_{\rm vac} \sim M_P^4 \sim 1$ with Planck units $c = \hbar = M_P = 1$, where Planck mass $M_P = \sqrt{\frac{\hbar c}{8\pi G}} = 2.43 \times 10^{18}$ GeV with the gravitational constant G. On the other hand, the observation value of Λ is $\Lambda_{\rm obs} \sim 10^{-120}$. This unreasonable deviation is called "cosmological constant problem". Introduced the decaying behavior of $\Lambda \propto t^{-2}$ as a function of time t is an inartificial solution. This is because, the present age of universe $t_0 = 1.37 \times 10^{10}$ years is expressed as $t_0 \sim 10^{60}$ with Planck units.

Scalar-tensor theory with Λ (STTΛ) [6] is the alternative gravitational theory which can solve the cosmological constant problem. In this theory, decaying Λ as t^{-2} is obtained as a result of spontaneous breaking of a conformal symmetry. It predicts a light scalar field "dilaton" as the NB boson as a result of the conformal symmetry breaking. Based on the prediction from STTΛ, dilaton has the extremely light mass $\sim 10^{-9} - 10^{-6}$ eV [7] and interacts with matter via extremely weak coupling as weak as that of gravity. In STTΛ, two photon coupling to a dilaton via quantum anomaly are allowed. Therefore, dilaton can be searched directly via the $\gamma\gamma \to \phi \to \gamma\gamma$ process, where γ and ϕ represent photon and dilaton, respectively. Dilaton has been searched indirectly by testing the deviation from the Newtonian gravity at short distances. For example, the modification to the Newtonian gravity as following form has been tested

$$V_r = -G\frac{m_1 m_2}{r}\left(1 + \alpha e^{-r/\lambda}\right), \tag{1}$$

where m_1 and m_2 are masses of samples, α is the strength of the hypothetical potential as compared to the Newtonian potential, and λ is its propagation length.

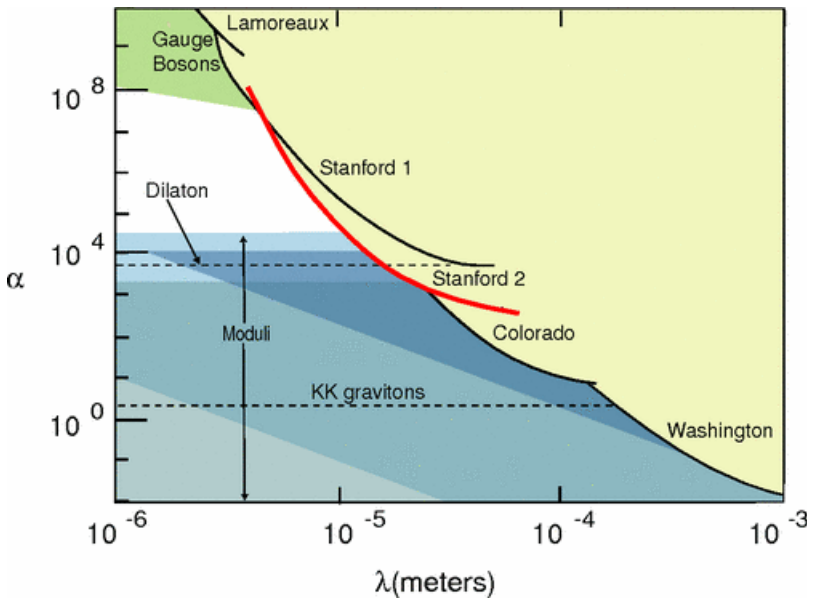

Figure 1. Exclusion limits for non-Newtonian forces in $\alpha - \lambda$ space [8]. The solid lines show upper limits obtained from previous experiments, Casimir force measurements "Lamoreaux"[9] and "Washington"[10], measurements of gravitational force between two bodies at short range "Stanford1"[11] and "Stanford2"[8], and measurement with torsion balance technique "Colorado"[12]. Shaded areas show the rough predictions for the dilaton based on the string theory [13], and KK gravitons which is predicted by extra dimension scenarios [14].

1.3 Search for pseudoscalar field, axion

The pseudoscalar field, "axion"[15, 16] is a possible candidate for cold dark matter [17, 18]. The expected mass scale of axion is $\sim 10^{-6} - 10^{-3}$ eV. Axion is a hypothetical boson introduced in order to solve "strong CP problem". In the QCD theory, the Charge conjugate - Parity (CP) symmetry is not guaranteed. Nevertheless, the CP violation in the QCD are strongly suppressed according to measurements of the electric dipole moment of neutron [19]. To solve this unnaturalness, an additional symmetry called "Peccei-Quinn (PQ) symmetry" [20] is introduced in the QCD Lagrangian. In this scenario, the CP symmetry is realized by spontaneous breaking of the PQ symmetry. As a result, axion appears as a Nambu-Goldstone mode.

Axion can also coupling to two photon as well as dilaton. Therefore axion (σ) has been searched via the $\gamma\gamma \to \sigma \to \gamma\gamma$ process by a number of experiments. For example, solar axion searches [21, 22, 23, 24, 25, 26, 27], searches via vacuum magnetic birefringence [28, 29, 30], light shining through a wall (LSW) [31, 32], and axion dark matter search (ADMX) [33, 34]. The exclusion limits for axion by previous searches are shown in Fig.2.

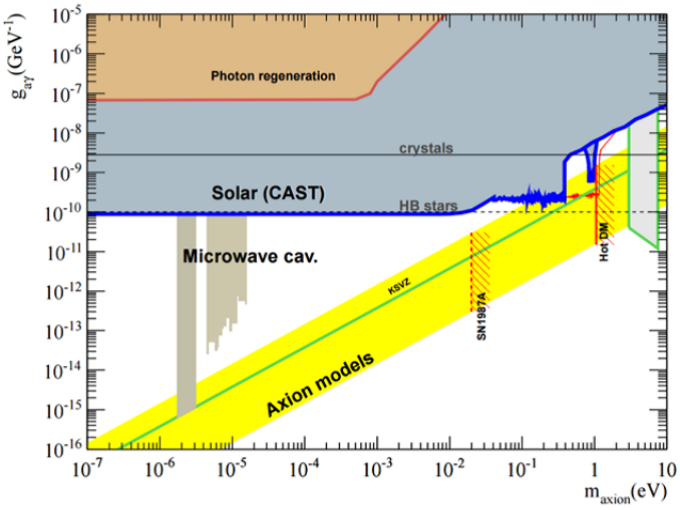

Figure 2. Exclusion limits for axion[35]. The horizontal and vertical axes indicate the mass of axion and the coupling constant between axion and photon, respectively. The brown area represents the exclusion limit by the LSW. The blue lines indicate the limit by the solar axion search experiments. The gray area shows the limit by the microwave cavity search like the ADMX. The yellow band represents the expected area of axion based on the prediction from the KSVZ axion model [36, 37].

Here the experimental strategy of LSW is introduced. The schematic view of experimental setup of LSW is shown in Fig.3.

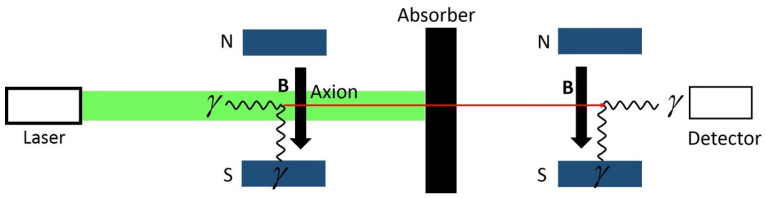

Figure 3. The schematic view of experimental setup of LSW

The LSW searches axion via the $\gamma\gamma \rightarrow \sigma \rightarrow \gamma\gamma$ process. Two photons at the initial state are provided from a laser and a external magnetic field. The photon propagating in the static magnetic field converts into the axion with a certain probability. The axion can be separated from laser photons by penetrating the absorber placed between two magnets and it converts into photon in the second magnetic fields.

The conversion probability of $\gamma \rightarrow \sigma \rightarrow \gamma$ is given by

$$P_{\gamma\rightarrow\sigma\rightarrow\gamma} \propto (gBL)^4 \left(\frac{1 - cos(qL)}{(qL)^2}\right)^2, \tag{2}$$

where $g = \alpha/M_a$ is a coupling constant of $\gamma - \sigma$, $\alpha \sim 1/137$ is the fine-structure constant and M_a is the energy scale parameter corresponding to the PQ symmetry breaking, B is the strength of the magnetic field, L is its length, q is the momentum difference between axion and photon.

1.4 Quasi parallel colliding system

Here a direct search for dilaton-like scalar fields and axion-like pseudoscalar fields by creating the resonance states of them in laboratory is discussed. Photon is a suitable probe for creating resonant states of extremely low mass fields due to zero mass of itself. At head-on photon-photon collisions, the colliding energy at the center-of-mass system $E_{\rm CMS}$ is expressed as 2ω, where ω is the energy of incident photons. When we assume optical photons whose energies are approximately 1 eV, we cannot capturing sub-eV mass resonances in head-on collisions.

Quasi parallel colliding system (QPS) [39, 40] is the system to realize the low colliding energy by colliding photons at small incident angles. The center-of-mass energy is expressed as

$$E_{\rm CMS} = 2\omega \sin\vartheta, \tag{3}$$

where ϑ is half of the incident angle of the photon pair. By introducing small ϑ, the colliding system to create resonances below sub-eV mass range is achieved. It is possible to realize the QPS by focusing a laser at a long focal length. In this method, search for scalar (ϕ) and pseudoscalar (σ) fields are performed by observing the $\gamma\gamma \to \phi/\sigma \to \gamma\gamma$ process.

In the QPS, the enhancement of the scattering rate is given by introducing another coherent field to stimulate the two photon decay of the resonance field. The initial and final state photons follow the energy conservation

$$\omega + \omega \to (2-u)\omega + u\omega, \tag{4}$$

where ω is the energy of photon which create a resonance, $u\omega$ is the energy of photon which induces the resonance decay with $0 < u < 1$. The photon whose energy is $(2-u)\omega$ is emitted as the signature of the resonance decay. The schematic view of the QPS is illustrated in Fig.4.

The similar relation in Eq.(4) is applied to the "four-wave mixing" process which is the third-order nonlinear quantum optical process in atoms [41, 42]. Therefore, search for low mass fields via QPS by combining two-color lasers is regarded as observing the four-wave mixing process in the vacuum. The four-wave mixing measurement in the vacuum is also used as a method for testing photon-photon scattering via nonlinear QED effects in different collision geometry [43, 44, 45, 46] .

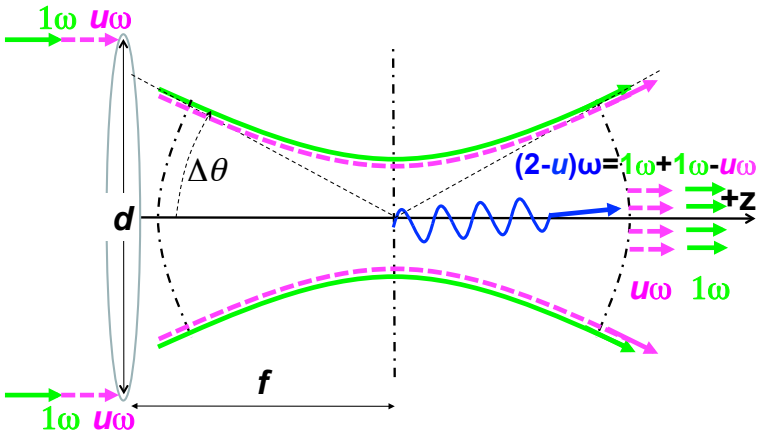

Figure 4. The schematic view of QPS. The photons to create resonance states are provided from the creation laser which is drawn by green. The inducing laser drawn by magenta induces the decay of resonances. The inducing laser is combined on the same optical axis of the creation laser. The parameters d, f, $\Delta\vartheta$ denote the beam diameter, the focal length, the upper range of incident angles of photons, respectively. The signal photon (blue) is emitted from the focal volume as a result of the exchanging of a resonance field via two photons scattering process [40].

The QPS has the characteristics that the signal yield has ${N_\gamma}^3$ dependence by the effect of the inducing mechanism, where N_γ is the number of photon per laser pulse. With taking the rapid developments of high intensity lasers into account, N_γ^3 dependence become prominent at experiments with higher intensity lasers. It encourage us to search unknown fields by QPS with laser fields.

1.4.1 Kinematics of QPS

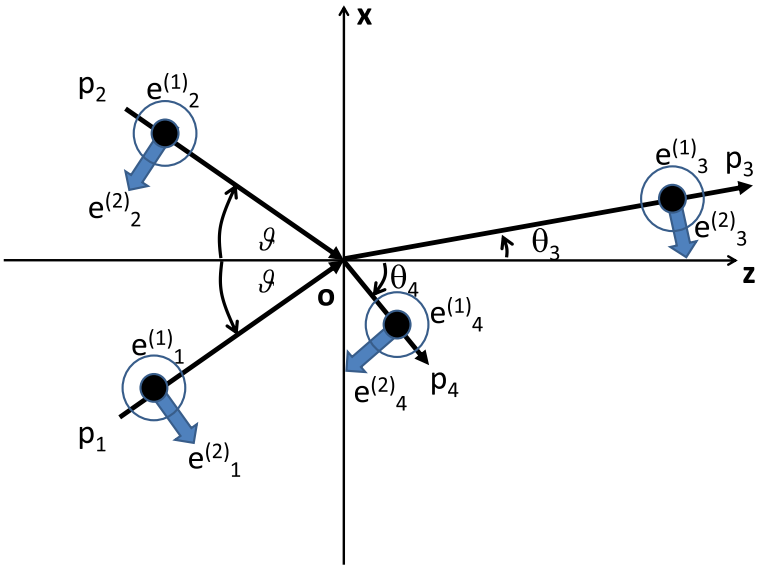

Figure 5. The definitions of kinematics variables in QPS [40].

The variables to describe the kinematics of QPS are introduced as illustrated in Fig.5. The 4-momentum vectors of incident photons p_1 and p_2 are defined on the z-x plane as follows:

$$p_1 = (\omega \sin\vartheta, 0, \omega\cos\vartheta; \omega), \tag{5}$$

$$p_2 = (-\omega \sin\vartheta, 0, \omega\cos\vartheta; \omega). \tag{6}$$

The energy conservation is expressed as

$$\omega + \omega = (2-u)\omega + u\omega, \tag{7}$$

where u is an arbitrary number which satisfies $0 < u < 1$. Then, the energies of final state photons are re-defined as follows:

$$\omega_3 \equiv (2-u)\omega, \tag{8}$$

$$\omega_4 \equiv u\omega, \tag{9}$$

where ω_3 and ω_4 are energies of a pair of final state photons The momenta of a pair of final state photons p_3 and p_4 are expressed as

$$p_3 = (\omega_3 \sin\theta_3, 0, \omega_3\cos\theta_3; \omega_3), \tag{10}$$

$$p_4 = (-\omega_4 \sin\theta_4, 0, \omega\cos\theta_4; \omega_4). \tag{11}$$

The relation of linear polarization states between initial and final state photons correlates the property of the exchanged resonance. In the case of scalar field exchange, the relations of linear polarizations when all wave vectors are on the same plane are expressed as

$$\begin{aligned} \omega\{1\} + \omega\{1\} &= \omega_3\{1\} + \omega_4\{1\}, \\ \omega\{1\} + \omega\{1\} &= \omega_3\{2\} + \omega_4\{2\}, \end{aligned} \tag{12}$$

where $\{1\}$ and $\{2\}$ denote linear polarization states orthogonal each other. In the case of pseudoscalar field exchange, the relations of linear polarizations are expressed as

$$\begin{aligned} \omega\{1\} + \omega\{2\} &= \omega_3\{1\} + \omega_4\{2\}, \\ \omega\{1\} + \omega\{2\} &= \omega_3\{2\} + \omega_4\{1\}. \end{aligned} \tag{13}$$

The linear polarization relations in Eq.(12) and Eq.(13) are applicable to the situation that all momentum vectors of photons are on the same reaction plane. In a focusing laser, the incident p_1-p_2 reaction plane and the outgoing p_3-p_4 plane rotate independently. Therefore, even if a $\{1\}$-polarized incident laser is provided at an actual experimental situation, the incident $p_1 - p_2$ plane rotates from the fixed $\{1\}$-polarized plane in the focal region. As a result, the focused QPS has sensitivity to both scalar and pseudoscalar fields simultaneously, even though we fix the linear polarization state of the incident laser before focusing. Hence, the sensitivities for scalar and pseudoscalar fields are evaluated by introducing the incident plane rotation factor $\mathcal{G}$. The evaluation of $\mathcal{G}$ is discussed in Appendix A of this thesis.

1.4.2 Mechanism for inducing effect

The Feynman diagram of the $\gamma\gamma \to \phi/\sigma \to \gamma\gamma$ process is shown in Fig.6. The effective interaction Lagrangians coupling between two photons and ϕ / σ are expressed as

$$-L_\phi = gM^{-1}\frac{1}{4}F_{\mu\nu}F^{\mu\nu}\phi, \quad -L_\sigma = gM^{-1}\frac{1}{4}F_{\mu\nu}\tilde{F}^{\mu\nu}\sigma, \tag{14}$$

where M is the energy scale parameter and g is the coupling constant, F is the electro magnetic tensor and $\tilde{F}$ is its duel.

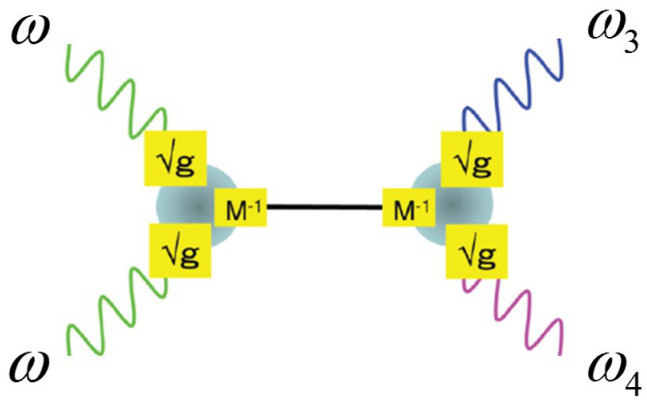

Figure 6. The Feynman diagram of the $\gamma\gamma \to \phi/\sigma \to \gamma\gamma$ process.

The photon-photon scattering probability is enhanced in the background coherent field as following mechanism. The Feynman amplitude of the $\gamma\gamma \to \phi/\sigma \to \gamma\gamma$ process as shown in Fig.6 is expressed as

$$V_2 \left((p_1 + p_2)^2 + m^2\right)^{-1} V_1. \tag{15}$$

where V_1 and V_2 are the matrix elements at the first and second vertices, respectively. Based on the interaction Lagrangian of the scalar filed exchange, V_1 and V_2 are expressed as

$$\begin{aligned} V_1 &= \frac{g}{M}\langle 0|F_{\mu\nu}|p_1\rangle\langle 0|F^{\mu\nu}|p_2\rangle, \\ V_2 &= \frac{g}{M}\langle p_3|F_{\mu\nu}|0\rangle\langle p_4|F^{\mu\nu}|0\rangle. \end{aligned} \tag{16}$$

We now simplify the expression of $\langle 0|F_{\mu\nu}|p_1\rangle$ as

$$\langle 0|a|p_1\rangle = 1, \tag{17}$$

by introducing the creation operator a and the annihilation operator $a^\dagger$. This description is applied in one photon state. In the case of coherent photons state, Eq.(17) substitute for

$$\langle\langle p_1, N|a|p_1, N\rangle\rangle = \sqrt{N}, \tag{18}$$

where N is the number of photons in the coherent state. In the case that the incident photons are provided from the coherent laser, V_1 is re-expressed as

$$V_1 = \frac{g}{M}\langle\langle p_1, N|F_{\mu\nu}|p_1, N\rangle\rangle\langle\langle p_2, N|F^{\mu\nu}|p_2, N\rangle\rangle. \tag{19}$$

It obtains the enhancement of N compared with Eq.(16). The similar enhancement mechanism can be applied at the second vertex V_2 when the inducing laser field is provided. If the momenta of inducing photons are equivalent to p_4, V_2 is expressed as follows:

$$V_2 = \frac{g}{M}\langle p_3|F_{\mu\nu}|0\rangle\langle\langle p_4, N|F^{\mu\nu}|p_4, N\rangle\rangle. \tag{20}$$

As compared to the second line of Eq.(16), V_2 in Eq.(20) obtains the enhancement of $\sqrt{N}$. Therefore the scattering rate has the enhancement of $\sqrt{N}^2 = N$ by the effect of the inducing laser field.

1.4.3 The effect of averaging the squared scattering amplitude

In general, the resonance of a particle is produced when the center-of-mass energy of a collision is equivalent to the mass of the resonance m. The mass of the resonance has the finite width duo to the uncertainty principle and the mass distribution takes the Breit-Wigner resonance distribution. At the Breit-Wigner distribution, the value of the full width at half maximum takes $\Gamma = \hbar/\tau$, where τ is the lifetime of the resonance. Therefore, the resonance condition is satisfied when E_{CMS} is included in the mass range of the resonance.

In the case of QPS, we now define the experimental parameters which satisfy the following resonance condition.

$$E_{\mathrm{CMS}} = 2\omega_r \sin\vartheta_r = m. \tag{21}$$

Based on the interaction Lagrangian at Eq.(14), the squared scattering amplitude in the s-channel $|\mathcal{M}_s|^2$ at the $\gamma\gamma \to \phi/\sigma \to \gamma\gamma$ process is expressed as

$$|\mathcal{M}_S|^2 \approx (4\pi)^2 \frac{a^2}{\chi^2 + a^2}. \tag{22}$$

with $\chi = \omega - \omega_r$.
a is defined as

$$a = \frac{\omega_r^2}{8pi}\left(\frac{gm}{M}\right)^2 = \frac{m\Gamma}{2\sin{\vartheta_r}^2}, \tag{23}$$

with

$$\Gamma = \frac{1}{16\pi}\left(\frac{g}{M}\right)^2 m^3. \tag{24}$$

When capturing the resonance of the low mass and weak coupling fields, the resonance width Γ becomes extremely narrow due to its small values of g/M and m. Hence, satisfying the resonance condition is quite difficult, if E_{CMS} takes a unique value at a individual collision like charged particle collisions. In the case of the off-resonance condition, in fact, $\chi \gg a$ duo to the small value of M^{-1}, $|\mathcal{M}_S|^2$ is strongly suppressed since $a^2 \propto M^{-2}$.

In QPS, however, the momentum vectors of photons fluctuate around their diffraction limit according to the uncertainty principle. The fluctuation appears as the uncertainty of the incident angle of photon ϑ. Therefore, E_{CMS} at QPS intrinsically has the uncertainty, even through it is a single collision. Thus, the quite narrow resonance can be captured if E_{CMS} includes the mass of the resonance in its fluctuation range.

Considering the uncertainty of the incident angles of the photons, the squared amplitude should be averaged over the possible incident angles as follows:

$$\overline{|\mathcal{M}_S|^2} = \int_0^{\pi/2} \rho(\vartheta)|\mathcal{M}_S(\vartheta)|^2 d\vartheta, \tag{25}$$

where $\rho(\vartheta)$ is the angler distribution of incident two photons in the Gaussian beam. $\rho(\vartheta)$ is expressed as

$$\rho(\vartheta) = \frac{2}{\sqrt{\pi}\Delta\theta} \exp\left\{ -\left(\frac{\vartheta}{\Delta\theta}\right)^2 \right\}, \tag{26}$$

where ϑ is the angle between a pair of incident photons, $\Delta\theta = d/2f$ is the possible maximum incident angle, and ϑ is given as

$$\vartheta = \frac{1}{2}|\theta_1 - \theta_2| \tag{27}$$

with the incident angle of single photon θ_1 and θ_2. Then, Eq.(25) is rewritten as follows:

$$\overline{|\mathcal{M}_S|^2} = \frac{(4\pi)^2}{\sqrt{\pi}\omega^2} \left(\frac{\vartheta_r}{\Delta\theta}\right) a\mathcal{W}, \tag{28}$$

with

$$\mathcal{W} \sim \frac{\pi}{2} \exp\left\{ -\left(\frac{\vartheta_r}{\Delta\theta}\right)^2 \right\}. \tag{29}$$

In Eq.(28), $\overline{|\mathcal{M}_S|^2}$ has a dependence but not a^2 dependence as shown in Eq.(22). We find that $a \propto M^2$ enhancement is obtained by operating the averaging process originating from the angler ambiguity of the incident photons. .

1.4.4 Coupling-mass relation

The signal yield $\mathcal{Y}$ is expressed with experimental parameters as follows:

$$\begin{aligned}\mathcal{Y} &= \frac{1}{64\sqrt{2}\pi^4}\left(\frac{\lambda_c}{c\tau_c}\right)\left(\frac{\tau_c}{\tau_i}\right)\left(\frac{f}{d}\right)^3 \tan^{-1}\left(\frac{\pi d^2}{4f\lambda_c}\right)\frac{(\overline{u}-\underline{u})^2}{\overline{u}\underline{u}} \\ &\times \left(\frac{gm[\mathrm{eV}]}{M[\mathrm{eV}]}\right)^2\left(\frac{m[\mathrm{eV}]}{\omega[\mathrm{eV}]}\right)^3 \mathcal{W}\mathcal{G}\mathcal{F}_s C_{\mathrm{mb}} {N_c}^2 N_i, \end{aligned} \tag{30}$$

where the subscripts c and i indicate the creation and inducing lasers, respectively, λ is the wavelength, τ is the pulse duration, f is the focal length, d is the beam diameter, $\overline{u}$ and $\underline{u}$ are the upper and lower values on u determined by the spectrum width of ω_4, respectively, $\mathcal{W} \sim \pi/2$ is the numerical factor relevant to the integral of the weighted resonance function, $\mathcal{G}$ is the incident plane rotation factor , $\mathcal{F}_{\mathcal{S}}$ is the polarization dependent axially asymmetric factor originated from rotation of $p_3 - p_4$ plane (the details of evaluations of $\mathcal{G}$ and $\mathcal{F}_S$ are described in Appendix A and B of this paper), $C_{\mathrm{mb}} = 1/2$ is the combinatorial factor originating from selecting a pair of photons among multimode frequency states and N is the average numbers of photons in the coherent state. The detail of the formulation of the signal yield is summarized in Appendix D of this paper. The coupling constant g/M is expressed as

$$\frac{g}{M[\mathrm{eV}]} = 2^{1/4}8\pi^2\sqrt{\frac{\mathcal{Y}\omega^3[\mathrm{eV}]}{\left(\frac{\lambda_c}{c\tau_c}\right)\left(\frac{\tau_c}{\tau_i}\right)\left(\frac{f}{d}\right)^3 \tan^{-1}\left(\frac{\pi d^2}{4f\lambda_c}\right)\frac{(\overline{u}-\underline{u})^2}{\overline{u}\underline{u}}\mathcal{W}\mathcal{G}\mathcal{F}_s C_{\mathrm{mb}} {N_c}^2 N_i}}\, m^{-5/2}[\mathrm{eV}]. \tag{31}$$

1.5 Four-wave mixing process in atoms

A four-wave mixing process is the nonlinear quantum optical process occurs via interactions between electric fields and matter. Atoms polarize when electric fields are applied. The polarizability of atoms have non-linearity in strong electric fields as follows:

$$\boldsymbol{P} = \epsilon_0(\chi^{(1)}\boldsymbol{E} + \chi^{(2)}\boldsymbol{E}^2 + \chi^{(3)}\boldsymbol{E}^3 + \cdots), \tag{32}$$

where $\boldsymbol{P}$ is the polarizability of atom, ϵ_0 is the permittivity of vacuum, $\chi^{(i)}$ is the i-th-order nonlinear susceptibility with $i = 1, 2, 3\cdots$, and $\boldsymbol{E}$ is the strength of the electric field. Incident photons induce an oscillating dipole moment in atom and the induced dipole moment radiates other photon fields.

The four-wave mixing is the third-order nonlinear process. The incident wave includes three separated frequencies, ω_1, ω_2, and ω_3 generates a new wave at ω_4 in polarized materials. The relation of the frequencies between incident and generated photons is expressed as

$$\omega_1 + \omega_2 - \omega_3 = \omega_4. \tag{33}$$

The energy diagram of the four-wave mixing process is drawn in Fig.7.

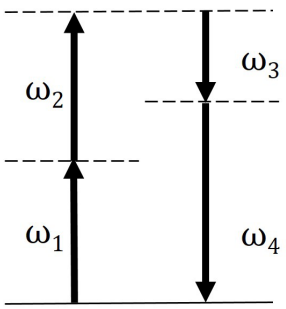

Figure 7. The energy diagram of four-wave mixing process.

When the frequencies of two absorbed photons have the relation of $\omega_1 = \omega 2$, this process is specially called "degenerate four-wave mixing", then, Eq.(33) is rewritten as

$$2\omega - \omega_3 = \omega_4, \tag{34}$$

with $\omega = \omega_1 = \omega_2$. This equation is similar to the energy conservation of the resonance production at QPS with two-colors laser fields expressed in Eq.(7). Therefore, the photons generated via the degenerate four-wave

mixing process in atoms can be the background source at the unknown fields search in QPS.

The intensity of the generated photon by the degenerate four-wave mixing process, $\omega_4 = 2\omega_1 - \omega_2$ at the plane waves condition is expressed [38] as

$$I_4 = \frac{576\pi^6 |\chi^{(3)}|^2}{{n_1}^2 n_2 n_4 {\lambda_4}^2 c^2} {I_1}^2 I_2 \frac{L^2 \sin^2(\Delta k L/2)}{(\Delta k L/2)^2}, \tag{35}$$

where I_i is the intensity of photons at frequency ω_i, n_i is the reflective index at ω_i, L is the interaction length, and Δk is the phase matching factor $\Delta k = k_4 - (2k_1 - k_2)$ with the wavenumber at ω_i.

I_4 has the cubic dependence of the strength of incident photon fields as $I_4 \propto {I_1}^2 I_2$, which is similar to the laser pulse energy dependence of the signal yields at the QPS with two-colors laser fields shown in Eq.(30).

1.6 Step-by-step searches in QPS

The concept for scalar and pseudoscalar fields search in QPS has been already advocated [39, 40]. However, the verification of the practical experimental approach is still developing. Therefore, thrashing out problems by increasing the laser intensities in step by step is important.

In QPS, the signal photon is emitted to the same optical axes of two-color lasers. Therefore, for example, if we use 1 J pulse laser, the signal photon has to be separated from $\sim 10^{18}$ photons per pulse. The optical system of QPS was developed for the first time at Hiroshima university in 2014 [48] . The schematic view of the optical system is shown in Fig.8.

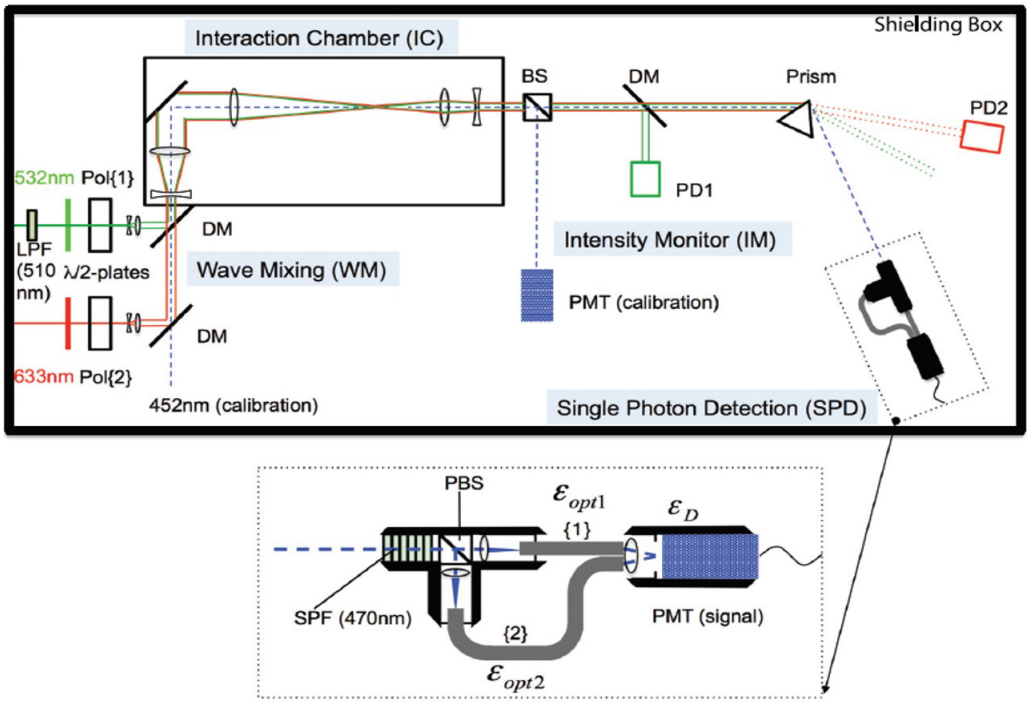

Figure 8. The schematic view of the experimental setup search for scalar fields by QPS [48].

We used a 0.2μJ/0.75 ns pulse laser as the creation laser which provides the initial photons create resonances and a 2 mW CW laser as the inducing laser which induces the decay of resonances. The wavelengths of the creation and inducing lasers are 532 nm and 633 nm, respectively. The wavelength of signal photon is 459 nm. Therefore, 452 nm CW laser is used as the

calibration source to determine the trajectory of the signal photon.

The creation and inducing lasers are combined by the dichroic mirror (DM) and they focused in the vacuum chamber. Then, both lasers are separated from signal waves by the prism and the photomultiplier tube (PMT) is placed on the trajectory of the signal photon. Optical filters to cut the creation and inducing photons are place in front of the PMT.

The scalar fields search was performed at 1.2×10^{-4} Pa with approximately 6.0×10^{-8} shot statistics. The leak photons from the creation and inducing lasers were suppressed at a level of less than 10^{-4} photons per pulse. Furthermore, no significant four-wave mixing signal is observed. From this pilot search experiment, It is confirmed that the experiment setup to detect the four-wave mixing signal with 1 photon sensitivity is feasible. Figure 9 shows the exclusion limit of scalar fields obtained at a 95% confidence level.

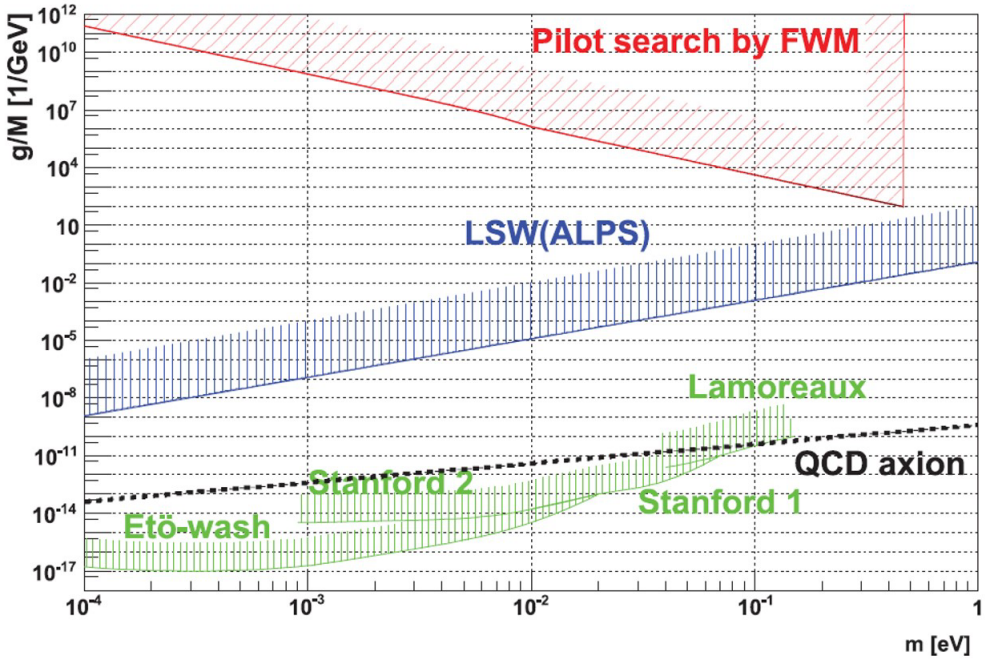

Figure 9. Exclusion limits for scalar fields are shown in m - g/M space [48], where m is the mass of the scalar field and g/M is the coupling constant to photon. The red shaded area indicates the exclusion limit by the pilot search by the QPS at a 95% confidence level. The blue shaded area represents the exclusion limit of scalar fields by LSW experiment "ALPS". The green shaded areas show the exclusion limits by non-Newtonian force measurements introduced in section 1.2. The expected line of axion is drawn by the black dotted line as a reference for future pseudoscalar search.

1.7 Aim of the thesis

The first search for scalar fields by QPS was performed with weak intensity lasers, thus, the effect of the four-wave mixing process in atoms was negligible. However, the atomic four-wave mixing process can be the main background source in the future search with higher intensity lasers.

In this thesis, a search experiment performed at Kyoto university with much higher beam intensities than that of the pilot search. In this experiment, the four-wave mixing photons originating from the residual gas are anticipated due to the higher beam intensities. This thesis gives the experimental methods to obtain the exclusion limits of scalar and pseudoscalar fields under the circumstance where a finite amount of background photons must be evaluated.

2 Experimental setup

2.1 Overview

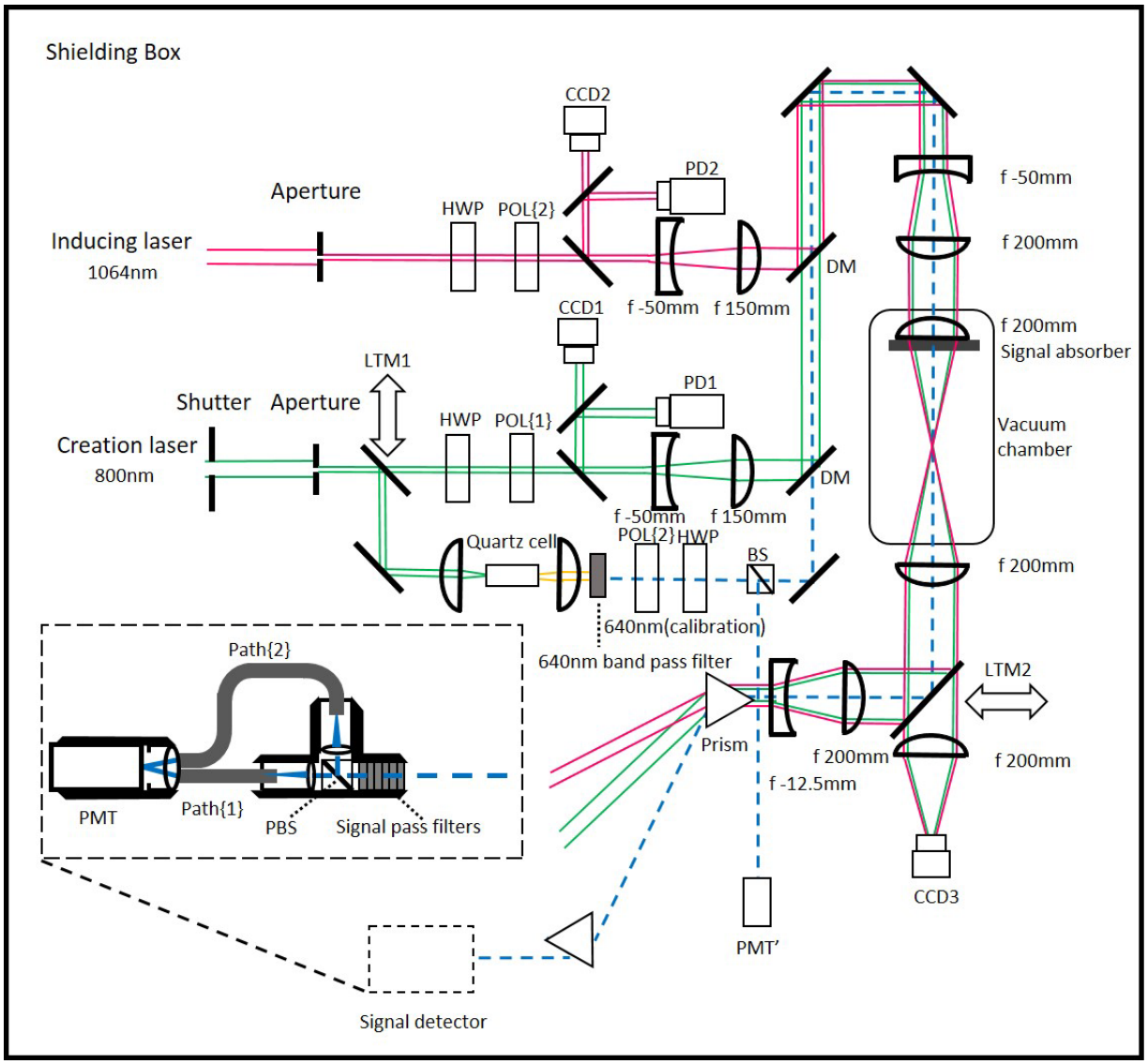

Figure 10. Schematic view of the experimental setup for the scalar and pseudoscalar fields search.

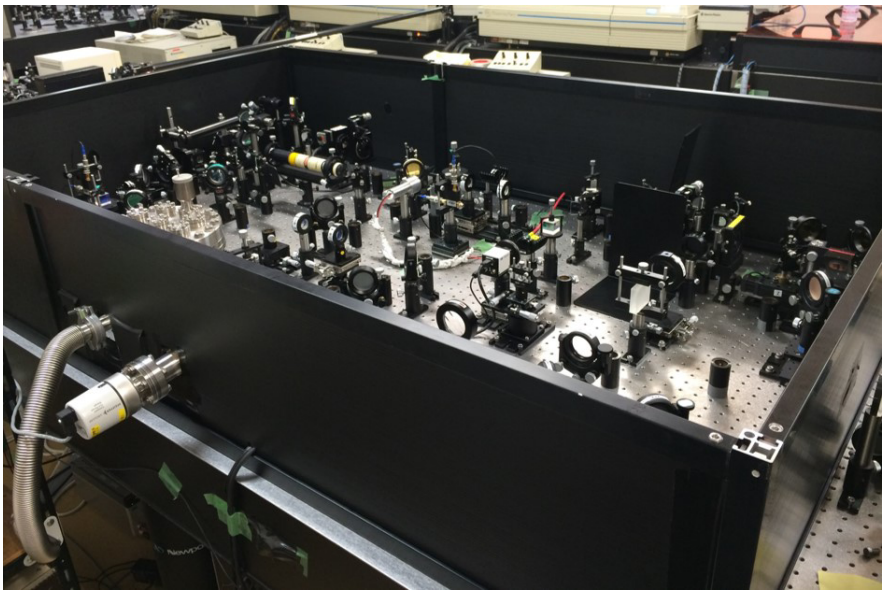

Figure 11. The picture of the optical systems.

Figure 10 illustrates the experimental setup for scalar and pseudoscalar fields search. A mode-locked Ti-sapphire laser, wavelength $\lambda_c = 800$ nm, and a Q-switched Nd:YAG laser, wavelength $\lambda_i = 1064$ nm are used as the creation and inducing lasers, respectively. The linear polarization states of the creation and inducing lasers are adjusted by polarization angles of the linear polarizers "POL{1}" and "POL{2}", respectively. POL{1} and POL{2} transmit only {1} and {2}-polarization components, respectively, where {1} and {2} are linear polarization states orthogonal each other. The half wave plate (HWP) placed on each beam line rotates the linear polarization angle of each beam, and rotation angles of them are fixed as transmitted lights from POL{1} and POL{2} are maximized.

The linear polarization vectors of the creation and inducing lasers are orthogonal because the number of the four-wave mixing photons in atoms are minimized when the polarization vectors of the two incident lasers are orthogonal each other. At this condition, the polarization relation between the initial and final state photons for the scalar field exchange in the focusing laser fields is expressed as

$$\omega\{1\} + \omega\{1\} = \omega_3\{2\} + \omega_4\{2\}. \tag{36}$$

In the case of the pseudoscalar field exchange, the relation is written as

$$\omega\{1\} + \omega\{2\} = \omega_3\{2\} + \omega_4\{1\}. \tag{37}$$

Thus, the polarization state of ω_4 depends on the property of the resonance.

Figure 12. The pictures of the creation laser (left: Hurricane, manufactured by Spectra-Physics) and the inducing laser (right: GCR350, manufactured by Spectra-Physics).

The beam profiles of the creation and inducing lasers are shaped to Gaussian-like profiles by going through the beam apertures with approximately 2mm clear apertures. Then a few percents of photons in lasers are split and the photo diodes "PD1" and "PD2" monitor the beam energies of the creation and inducing lasers, respectively, and CCD cameras "CCD1" and "CCD2" monitor the beam alignments of them, respectively.

The beam diameters of them are expanded to approximately 5 - 6 mm by the telescope on each beam line, and they are combined with the dichroic mirror (DM) and the beam diameters are expanded to approximately 20 mm by the common telescope. The combined beam is guided into the vacuum chamber and focused by the convex lens at a 200 mm focal length.

The signal absorber consists of five optical filters which absorb below 750 nm wavelength photons is placed in front of the convex lens in the vacuum chamber. It eliminates the background photons emitted from the optical components.

The agreement of the optical axes between the creation and inducing lasers are ensured at a precision of 2-3 μm by adjusting the focal spots of them at the near side and the far side of the interaction point with CCD camera.

The center of wavelength of the signal photon λ_s is evaluated as

$$\lambda s = \frac{\lambda i \lambda c/2}{\lambda i - \lambda c/2} = 641\text{nm}. \tag{38}$$

To make sure the detection efficiency and the trajectory of the signal photons, the calibration light, $\lambda = 640$ nm, is combined to the same optical axes of the creation and inducing lasers. The 640nm calibration light is pick up from the white light source created by "self phase modulation (SPM)", which is the third-order nonlinear quantum optical effect occurring by alteration in the refractive index which has the dependence of the electric field strength. Now SPM effect is given by focusing the creation laser to the quartz cell target filled with water as shown in Fig.13. As a result, the energy spectrum of the creation laser has a broadening effect by SPM. The 640nm light is obtained from the white light source by placing the band pass filter which transmits 640 ± 5 nm photons. The beam splitter (BS) splits the calibration light evenly and the photomultiplier tube (PMT') monitors the beam energy of the calibration light. Whether the creation laser is guided into the vacuum chamber or the quartz cell to produce the calibration light is selected by switching the linear translation mirror (LTM1).

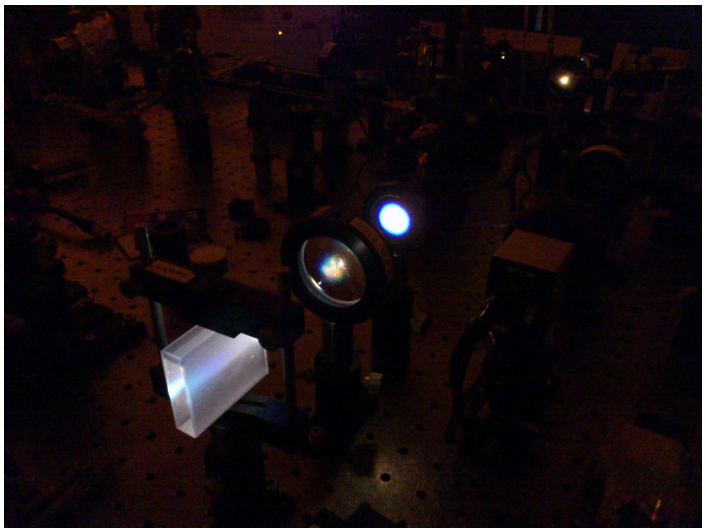

Figure 13. White light is emitted by focusing the creation laser in the quartz cell filled with water.

The linear translation mirror (LTM2) switches the beam line of the combined beam whether the beam goes to the signal detector or the CCD camera (CCD3). The agreement of the focal spots of the creation and inducing lasers are confirmed by monitoring the images of beam spots by CCD3 before and after the physics run.

The combined beam and signal photons are separated by a pair of prism

and the signal detector is placed on the trajectory of the signal photons.

The signal pass filters which transmit 580 - 690 nm wavelength photons are set to eliminate residual photons from the creation and inducing lasers. The polarization beam splitter (PBS) split the signals to {1}- polarized and {2}-polarized components, respectively. The {1}-polarized and {2}-polarized signals through the short (Path{1}) and the long (Path{2}) optical fiber paths, respectively, with having a 23ns of time delay. Then photons from each path enter a common photo device. A single-photon-sensitive photomultiplier tube (PMT; R7400-01, manufactured by HAMAMATSU) is used as the signal detector.

2.2 Data acquisition trigger

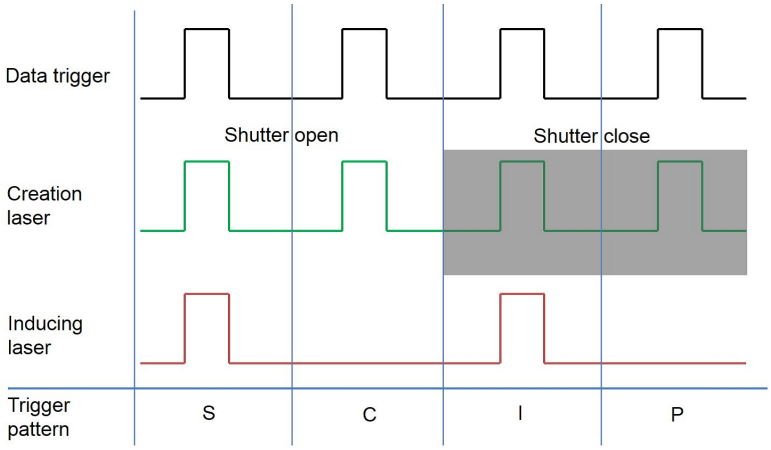

Figure 14. The image of the trigger logic

The repetition rate of the creation and inducing lasers are 1 kHz and 10 Hz, respectively. The coincidence of the pulse timing of them is adjusted so that the yields of the four-wave mixing photons emitted from gas in the focal volume are maximized. The shutter is placed on the beam line of the creation laser and it repeats open and close every 5 seconds. The image of the trigger logic is illustrated in Fig.14. The 20 Hz data acquisition trigger synchronizes to both pulses and it makes four trigger patterns, which are "the both lasers are incident (S)", "only the creation laser is incident (C)", "only the inducing laser is incident (I)", and "neither lasers is incident (P)". A digital oscilloscope records the waveform data from PD1, PD2 and PMT triggered by the data acquisition trigger.

3 Waveform analysis

3.1 Peak finding algorithm

The recorded waveform data from the PMT consists of 500 sampling points p_1 - p_{500} in 200 ns time range. Peak structures originating from observed photons are searched by a peak finding algorithm. The algorithm is operated as following steps:

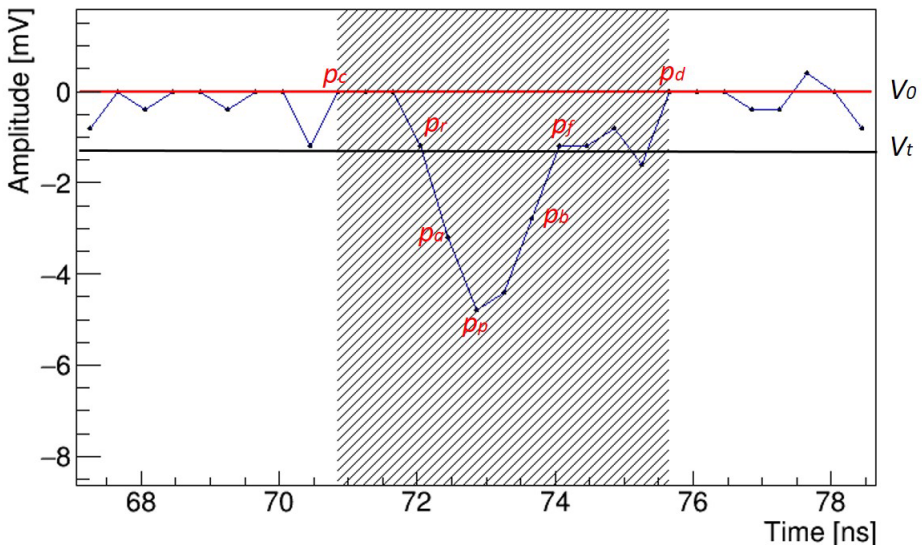

Figure 15. The waveform example to show peak finding procedures. The red horizontal line indicates the pedestal value and the black horizontal line means the threshold value for peak finding. The gray shaded area shows the integral range to evaluate the charge sum.

1. The pedestal value V_0 is defined as the average voltage of p_1 - p_{100} and p_{400} - p_{500}.
2. Set a threshold voltage V_t and search points p_a and p_b satisfy the following requirements:
   $V_\mathrm{t} - V_0 < V_{p_{(\mathrm{a}-1)}}$ and $V_{p_\mathrm{a}} \geq V_\mathrm{t} - V_0$,
   $V_\mathrm{t} - V_0 \leq V_{p_\mathrm{b}}$ and $V_{p_{(\mathrm{b}+1)}} > V_\mathrm{t} - V_0$.
3. Find the point p_p which has the minimum voltage from p_a to p_b and regard p_p as a peak point.
4. Search points p_r and p_f which satisfy following conditions:
   $1/2(V_{p_\mathrm{p}} - V_0) \geq V_{p_\mathrm{r}}$ and $V_{p_{(\mathrm{r}+1)}} < 1/2(V_{p_\mathrm{p}} - V_0)$,
   $1/2(V_{p_\mathrm{p}-V_0)} < V_{p_{(\mathrm{f}-1)}}$ and $V_{p_\mathrm{f}} \geq 1/2(V_{p_\mathrm{p}} - V_0)$.
5. Define points p_c and p_d as below:
   $\mathrm{c} = 2(\mathrm{p} - \mathrm{r}) - 1$ and $\mathrm{d} = 2(\mathrm{f} - \mathrm{p}) + 1$.

Then, the peak structure is defined as data points from p_c to p_d. The charge sum of the peak structure Q is calculated as

$$Q = \sum_{n=c}^{d} \frac{(V_{p_\mathrm{n}} - V_0)\,\Delta t}{R}, \tag{39}$$

where $\Delta t = 0.4$ ns is the time interval between V_n and $V_{\mathrm{n}+1}$, and $R = 50\ \Omega$ is the impedance. The charge sum of the peak structure is converted into the unit of the number of photons by dividing it from the single-photon equivalent charge.

3.2 Noise event subtraction

The recorded data contains some noisy waveforms originating from the ambient noises in the laboratory. These noisy waveforms should be removed before search photon-like peaks because the noises could be misidentified as photon-like peak structures.

The noisy waveforms are identified by analyzing the frequencies of the waveforms since the frequencies of noise events tend to be lower than those of normal events. The frequencies are estimated by counting the nodes, which is defined as the intersection between a waveform and the average line of amplitudes within the 200ns time window.

Figure 16 shows the distributions of the number of nodes for trigger patterns S, C, I, and P. A waveform the number of node is lower than 150

is defined as a noise event. The typical waveforms identified as noisy and normal events are shown in Fig.17.

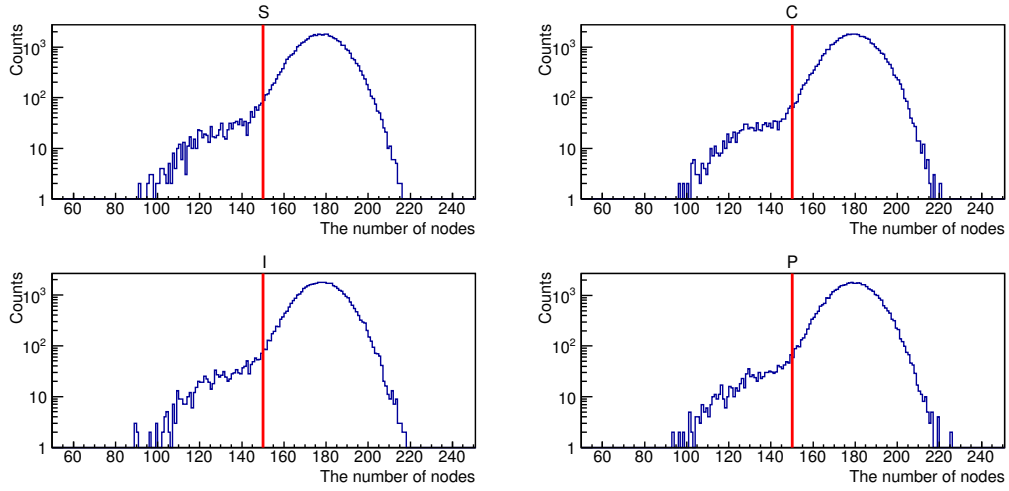

Figure 16. The distributions of the number of nodes for trigger patterns S, C, I, and P [47]. The red vertical lines indicate the boundary of 150 nodes. All trigger patterns have similar distributions.

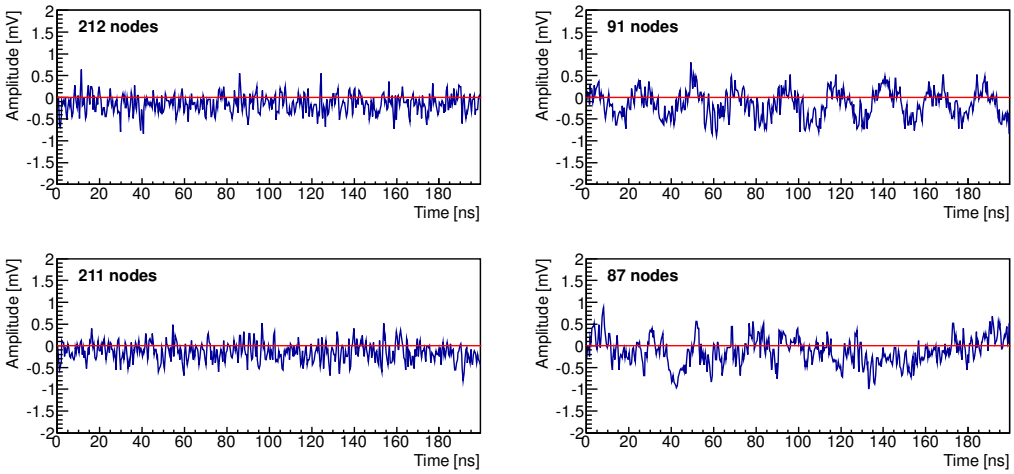

Figure 17. The two panels on the left and right sides show the example of waveforms identified as normal and noise events, respectively [47]. The red horizontal lines indicate the averages of the amplitudes of 500 sampling points in each waveform.

3.3 Trigger pattern selection

The beam energies of the creation and inducing lasers are monitored by photo diodes PD1 and PD2, respectively. The trigger pattern is classified according to the charge correlation between the waveforms from PD1 and PD2. The waveform examples from PD1 and PD2 are shown in Fig.18 and Fig.19, respectively.

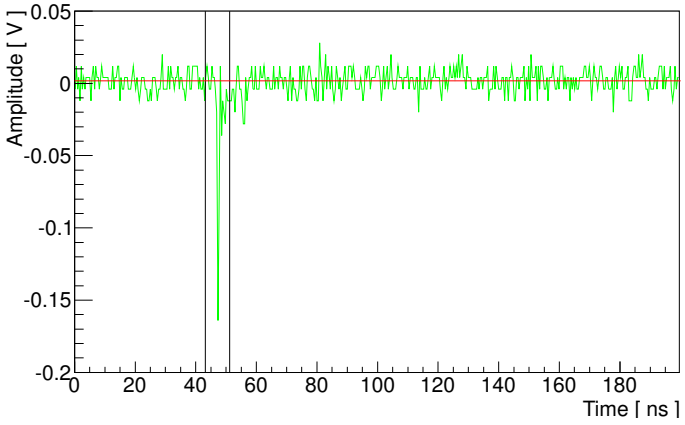

Figure 18. The waveform example from PD1. The red horizontal line indicates the pedestal line. The black vertical lines show the integral range for evaluating the charge sum.

The charge sum of the creation laser Q_c is evaluated as

$$Q_c = \sum_{t=\mathrm{a}}^{\mathrm{b}} \frac{(V_{p_\mathrm{t}} - V_0)\,\Delta t}{R}, \tag{40}$$

where a = 43.2 nm and b = 51.2 nm are integral ranges for all waveforms from PD1, and V_0 is the pedestal value evaluated for event by event as the average of amplitudes from 1 - 100 and 400 - 500 data points.

The charge sum of the inducing laser Q_i is evaluated as integral of the amplitudes over 1 - 500 points.

The recorded waveforms from PMT are tagged with trigger patterns S, C, I, or P. Which pattern the waveform belongs to is determined by the charge correlation between PD1 and PD2 shown in Fig.20.

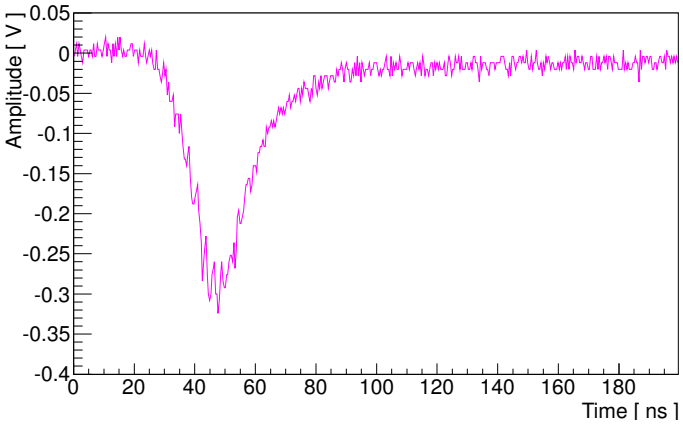

Figure 19. The waveform example from PD2.

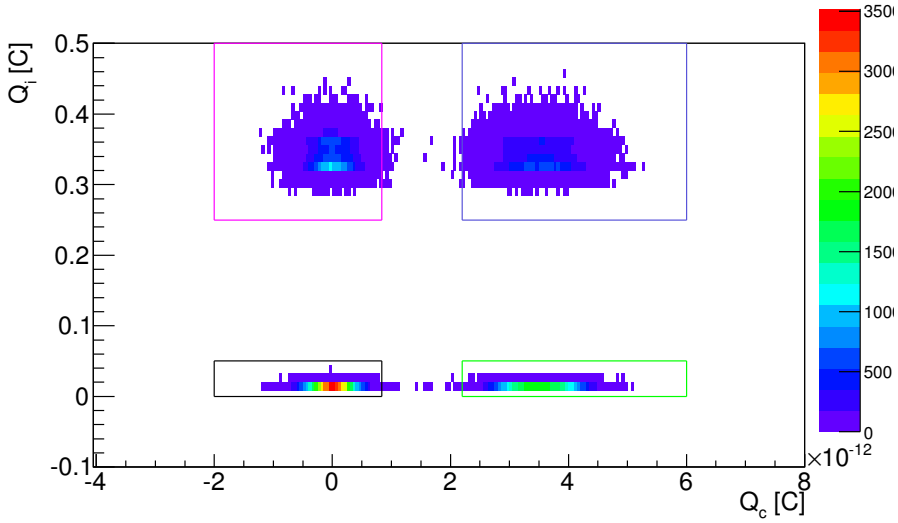

Figure 20. The distributions of charge correlation between the creation and inducing lasers. The data points in the blue, green, magenta and black rectangles indicate trigger patterns S, C, I and P, respectively.

Table 1 shows the number of events for each trigger pattern in the physics run.

Table 1: Data table for the number of events in each trigger pattern

Trigger pattern	The number of events
S	46120
C	46203
I	46044
P	46169

3.4 Threshold value for peak identification

The threshold value V_{t} for identifying the photon-like peak is determined by checking the correlation between V_{t} and the charge sum of peak structures shown in Fig.21. From Fig.21, V_{t} becomes lower, the negative charge value increase. These negative charges are come from misidentifying the noise as peak structures. Therefore, the effectual threshold value should be set to the region the negative charges are not contained. Therefore, $V_{\mathrm{t}} = -1.3$ mV is given as the effectual threshold value.

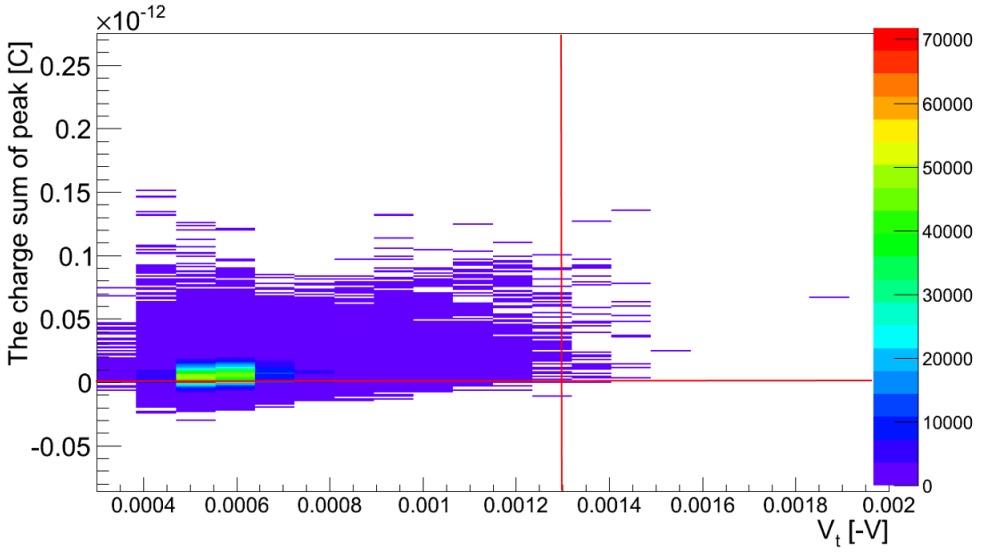

Figure 21. The correlation between V_{t} and the charge sum of peak structures. The red horizontal line shows 0 charge line and the red vertical line indicates the adopted threshold value $V_{\mathrm{t}} = -1.3$ mV.

3.5 Signal-like peak position

The photons which propagate from the focal spot to the detection point make the characteristic peak structures at specific time domains. The time domains that signal expected be observed are determined by observing the four-wave mixing photons emitted from gas in the focal volume. Figure 22 shows the time distributions of observed photons at 5.0×10^4 Pa.

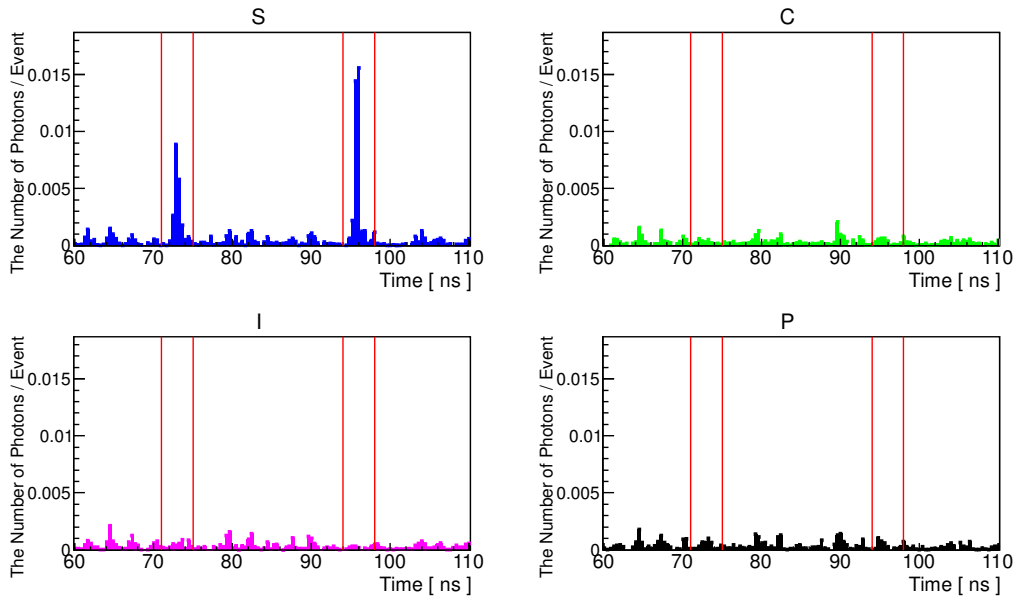

Figure 22. The time distributions of observed photons (efficiency-uncorrected) per triggered event at 5.0×10^4 Pa [47]. The left and right bands bounded by two neighboring vertical lines indicate the time domains $T\{1\}$ and $T\{2\}$ where $\{1\}$ and $\{2\}$-polarized photons are expected to be observed. The signal-like peaks are observed only in S-pattern.

The time domains in 71-75 ns ($T\{1\}$) and 94-98 ns ($T\{2\}$) indicate the arrival times of $\{1\}$ and $\{2\}$-polarized photons traveling the short optical fiber path Path$\{1\}$ and the long optical fiber Path$\{2\}$, respectively. The relative time difference between $T\{1\}$ and $T\{2\}$ is 23 ns. It is consistent with the time difference between Path$\{1\}$ and Path$\{2\}$.

4 Detector calibration

4.1 Evaluation of 1 photon equivalent charge

To convert the charge sum from the PMT into the number of photons, the 1 photon equivalent (1 P.E.) charge of the PMT has to be evaluated. The 1 P.E. charge was measured with a 532 nm pulse laser in advance of the search experiment. It is assumed that the charge distributions consist of multiple Gaussian distributions corresponding to the incident photon counts. The charge distributions are fitted by multiple Gaussian distributions based on following assumptions:

- The 0 photon distribution does not correlate with the finite photons distributions.
- $\mu_N - \mu_0$ is proportional to the number of incident photons N. Where μ_N is the mean of the N photons distribution.
- The variance of the N photons distribution σ_N^2 is proportional to the number of incident photons N.
- The incident photon counts conform to Poisson distribution.

Therefore, the multiple Gaussian fitting is operated as we fix the free parameters μ_0, σ_0, μ_1, and σ_1.

The 0 photon distribution is determined by recording waveform data without photon injection. The charge distribution with 45000 statistics are shown in Fig. 23. From the fitting gauss function,

$$\mu_0 = -2.785 \times 10^{-15}, \tag{41}$$
$$\sigma_0 = 1.090 \times 10^{-14} \tag{42}$$

are given.

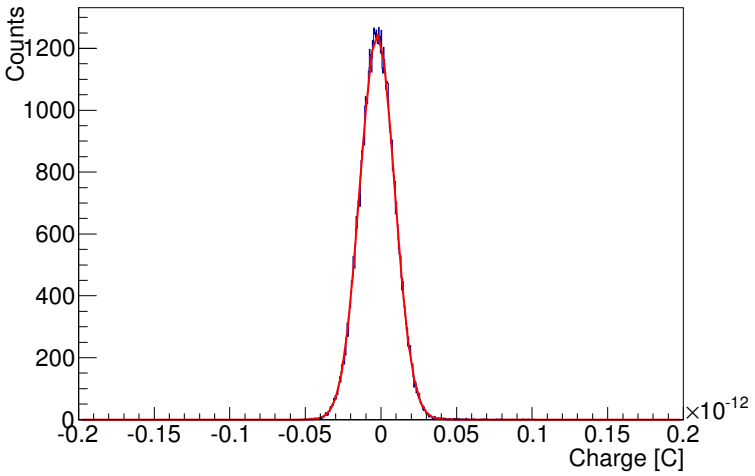

Figure 23. The charge distribution without photon injection.

Then, the intensity of the incident laser is adjusted to extremely low to determine the 1 photon distribution. The intensity of the laser becomes higher, the contribution of 1 photon distribution is clearly appeared as right side tail of the charge distribution. The obtained charge distributions are fitted by 0 photon + 1 photon + 2 photon distributions by increasing the laser intensity moderately. μ_0 and σ_0 are fixed and the other μ_N and σ_N are given as free parameters at this time.

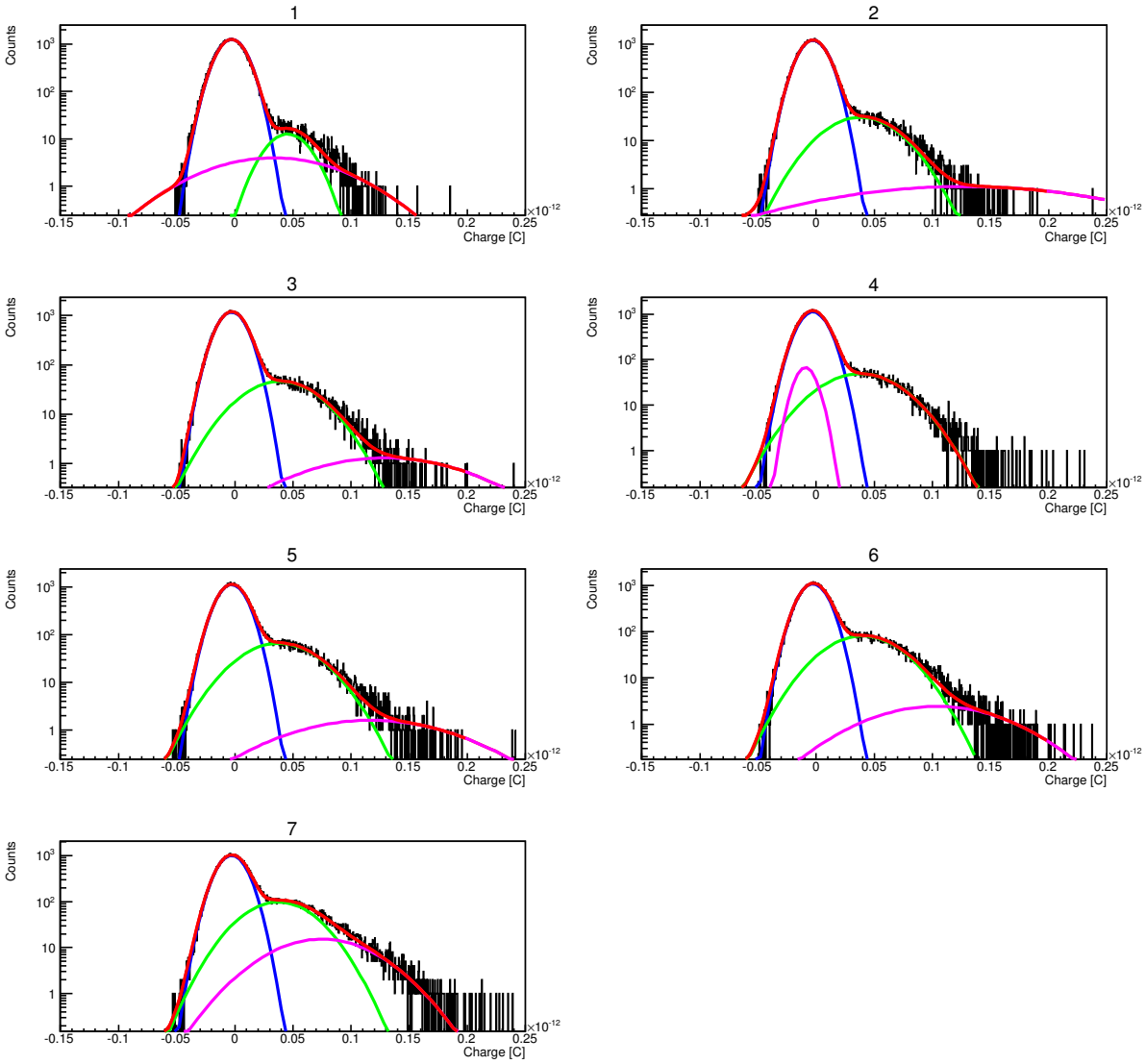

Figure 24. The charge distributions fitted by 3 Gaussians. The blue, green, and magenta lines represent 0,1, and 2 photon(s) distribution, respectively. The red line shows the sum of 3 Gaussians.

The fitting parameters of the 1 photon distribution should not fluctuate by changing of the laser intensity. The laser intensity dependence of μ_1 and σ_1 are shown in Fig.25. The fluctuations of μ_1 and σ_1 are converged from No.2 to No.7. Thus, we evaluate μ_1 and σ_2 as the average values in these range,

$$\mu_1 = 3.838 \times 10^{-14}, \quad (43)$$

$$\sigma_1 = 2.807 \times 10^{-14}. \quad (44)$$

.

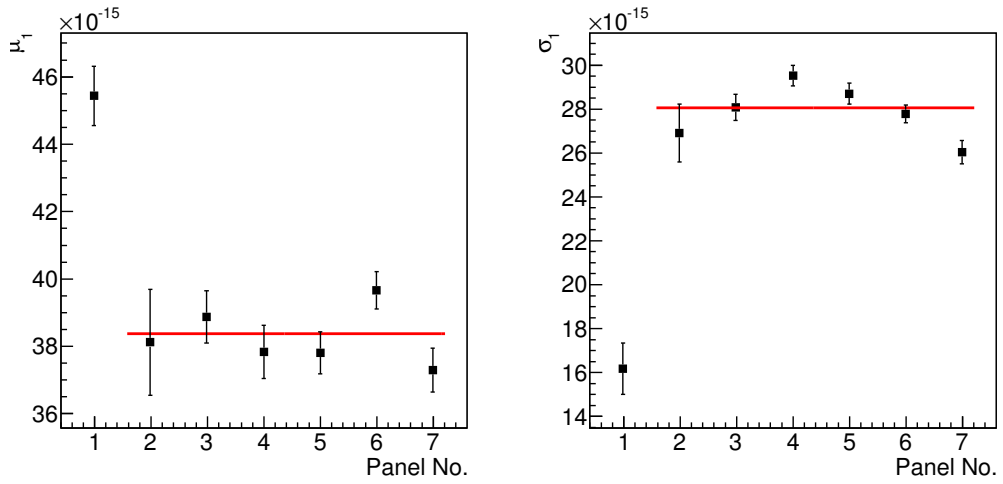

Figure 25. The laser intensity dependence of μ_1 and σ_2 are shown at the left and right panels, respectively. The integer numbers in x-axis indicate the corresponding panel No. in Fig. 24. The red horizontal lines stand for the average value from No.2 to No.7.

Then, the charge distributions are fitted by the multiple Gaussians at the higher intensities setting. Now μ_N and σ_N become fix parameters, thus, the multiple Gaussian fitting function are given uniquely by calibrating the average number of incident photons λ. The best suited value of λ are determined when the minimum χ^2 are given. Figure 26 shows the charge distributions fitted by multiple Gaussian functions.

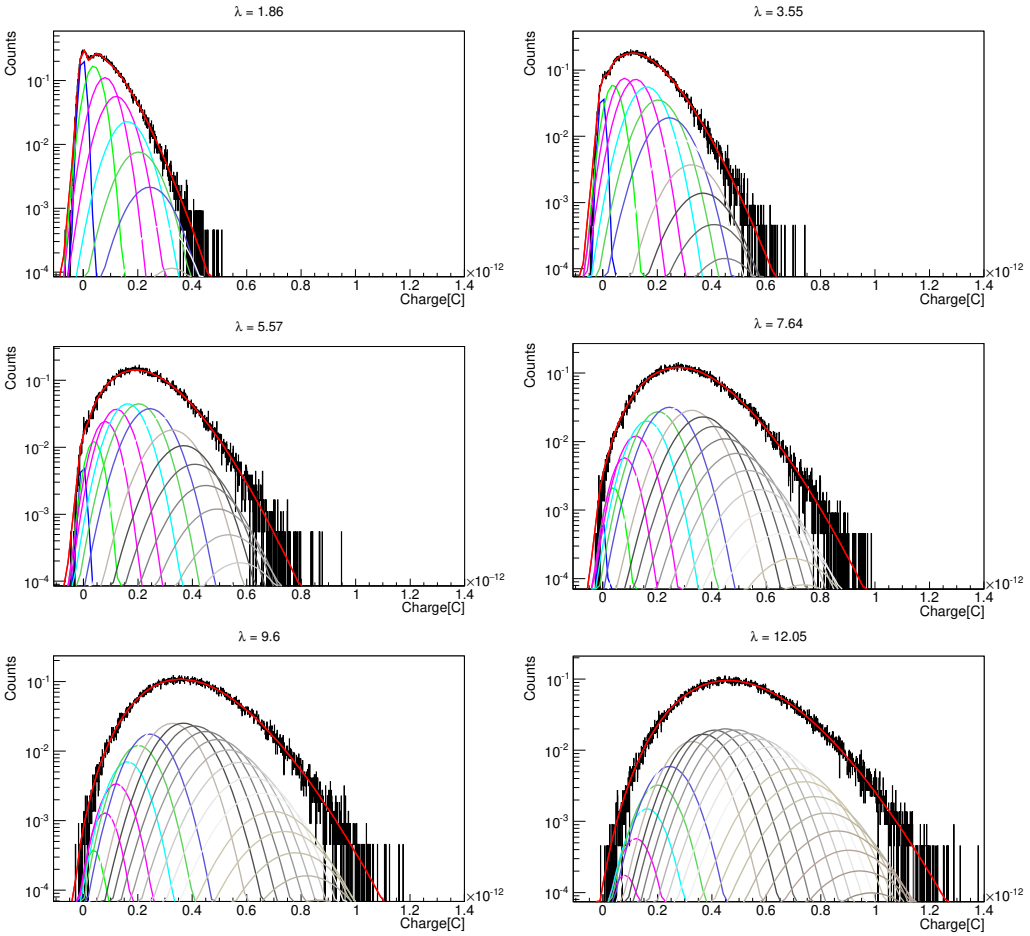

Figure 26. Charge distributions fitted by multiple Gaussians at the higher intensities setting.

The correlation between λ and the mean value of the charge distributions are shown in Fig.27 with the fitting linear function. The charge mean are proportion to the average number of incident photons λ. Finally, the 1 photon equivalent charge $Q_{\text{p.e.}}$ is given as the slope of the linear function as

$$Q_{\text{p.e.}} = 4.13 \pm 0.06 \times 10^{-14} \text{ C}. \tag{45}$$

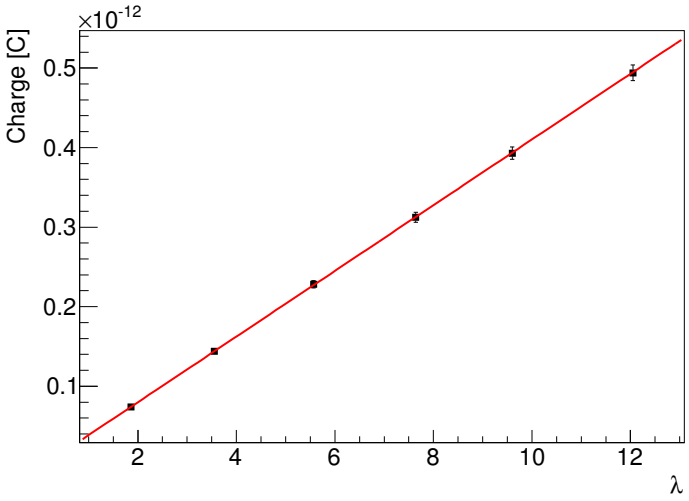

Figure 27. The correlation between λ and the mean value of the charge distributions

4.2 Detection efficiency

The detection efficiency of the PMT is evaluated by comparing the number of observed photons at the PMT and the power of the incident laser by using a 532nm pulse laser. The measurement setup is shown in Fig.28.

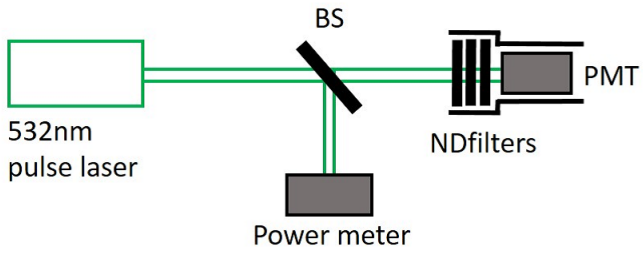

Figure 28. Setup to measure the detection efficiency of the PMT

The pulse laser is split to two optical paths evenly by a beam splitter (BS). The power of incident laser is measured by a calibrated power meter. The laser at another path is attenuate by three optical filters (ND filters) and guided to the PMT.

The average power of the incident laser measured by the power meter is 1.09 ± 0.01 mW. The pulse energy is evaluated to 55.1 ± 0.5 nJ by taking the repetition rate of the incident laser 19.8 Hz into account. The number of photons per pulse N_{PM} is evaluated as

$$N_{\mathrm{PM}} = (1.49 \pm 0.01) \times 10^{11}. \tag{46}$$

N_{PMT}, the number of observed photons at the PMT, is given by converting the average value of the charge distribution from the PMT.

$$N_{\mathrm{PMT}} = 16.0 \pm 0.1. \tag{47}$$

Then attenuation factor of three optical filters placed in front of PMT are measured as

$$\xi = 4.6 \times 10^{-9}. \tag{48}$$

The detection efficiency ϵ_D is calculated as follows:

$$\epsilon_D = \frac{N_{\mathrm{PMT}}}{\xi N_{\mathrm{PM}}} = 2.4 \pm 0.1\ \%. \tag{49}$$

5 Experimental parameters

5.1 Beam diameters

The beam diameters of the creation and inducing lasers before expanded by telescopes are measured by CCD cameras directly.

The x-y beam profile of the creation laser averaged 50 pulses is shown in upper-left of Fig.29. The beam diameter is determined by fitting the 3D beam profile by the 2D gauss function shown in upper-right of Fig.29. The fitting function forms

$$f(x,y) = A\exp\left(-\frac{(x-\mu_x)^2}{2\sigma}\right)\exp\left(-\frac{(y-\mu_x)^2}{2\sigma}\right) + C, \tag{50}$$

where A is the amplitude, C is the offset, μ_x and μ_y are the mean values in x and y axis, respectively, and σ is the standard deviation. The common σ is applied in x and y axes due to making the parametrization simply in the QPS.

The under-left and under-right panels in Fig.29 show x and y projections fitted by the 2D gauss function, respectively. The similar plots in the case of the inducing laser are shown in Fig.30.

The beam diameters of the creation and inducing lasers d_c and d_i are defined as 2σ of the 2D gauss function. As a result,

$$d_c = 1.64 \pm 0.01 \text{ mm}, \tag{51}$$
$$d_i = 1.69 \pm 0.01 \text{ mm} \tag{52}$$

are obtained, where the unit of [pixel] are converted into [mm] by taking a 11.2 μm pixel size of the CCD camera into account .

Both beam are expanded 3 times lager by the telescopes and further expanded 4 times larger after they are combined. The expanded beam diameters of the creation and inducing lasers D_c and D_i are estimated as

$$D_c = 19.6 \pm 1.6 \text{ mm}, \tag{53}$$
$$D_i = 20.3 \pm 1.7 \text{ mm}, \tag{54}$$

respectively, with taking the total enlargement factor 12 ± 1 into account.

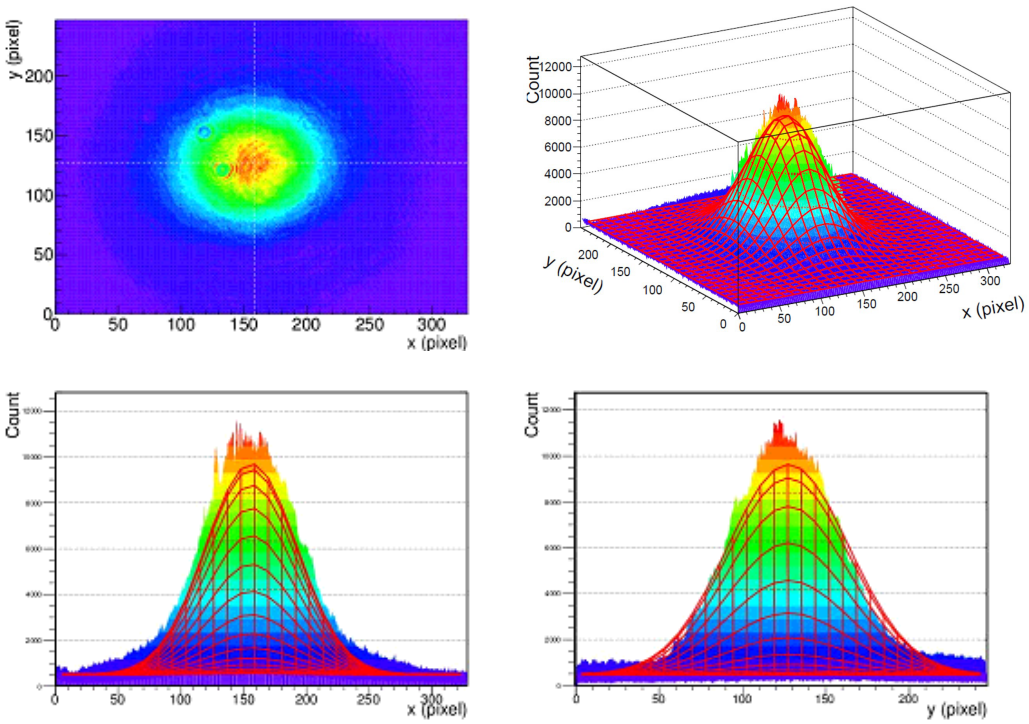

Figure 29. The beam profile of the creation laser

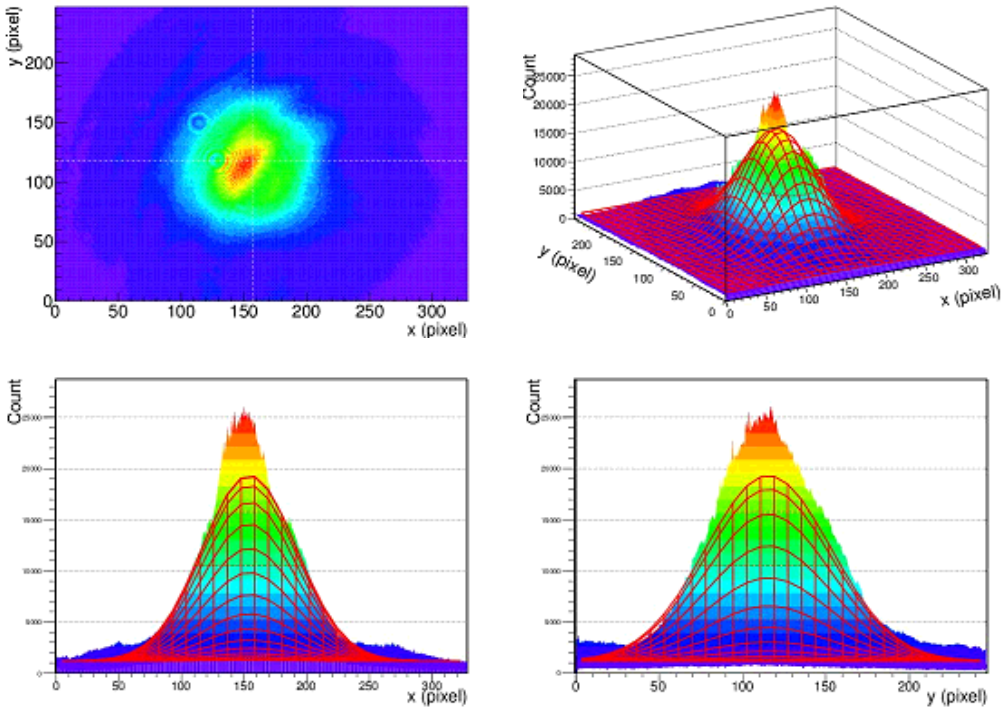

Figure 30. The beam profile of the inducing laser

5.2 Beam overlapping factor at the focal spot

The number of photons contribute to the inducing mechanism in the inducing laser should be considered. It estimated by measuring how much beam energies of the creation laser overlap to that of the inducing laser at the interaction point in the vacuum chamber. Since the correction of this overlapping factor are most sensitive around the focal spot.

The beam profiles of the creation and inducing lasers at the focal spot are measured at the interaction point by the common CCD camera. The incident beams are expanded by the telescope installed in front of the CCD camera due to the small size of images captured at the focal spot.

The x-y projection of the creation and inducing beams are shown in Fig.31. The spot size of them are defined as well as in the case of determining the beam diameter of them. The common mean values of the 2D gauss function μ_x and μ_y are assigned to the beam profiles of the creation and the inducing lasers.

The measured spot diameters of the creation and inducing lasers are $20.9\pm$ 0.1 μm and 23.1 ± 0.1 μm, respectively. A ideal spot diameter of a coherent Gaussian beam d_{f} is evaluated as

$$d_{\mathrm{f}} = \frac{4\lambda f}{\pi d}. \tag{55}$$

From Eq.(55), the spot diameters of the creation and inducing lasers are evaluated as 10μm and 12μm, respectively. The measured spot diameters are broadened compared with the ideal values due to the incoherence of the beams come from their intrinsic properties and the effect of optical materials.

The beam energy overlapping factor

$$\eta = 0.87 \tag{56}$$

is evaluated by integrating the counts in the beam profiles of the inducing laser over the area that the spot of the creation laser covers.

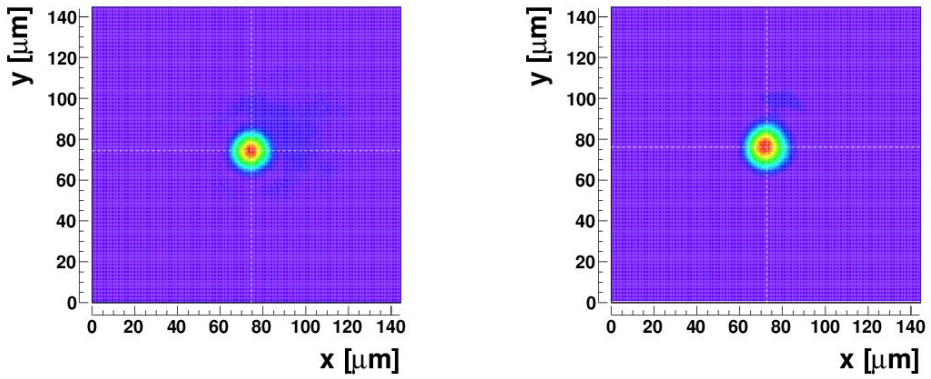

Figure 31. The beam profiles of the creation (left) and inducing (right) lasers at the focal spot

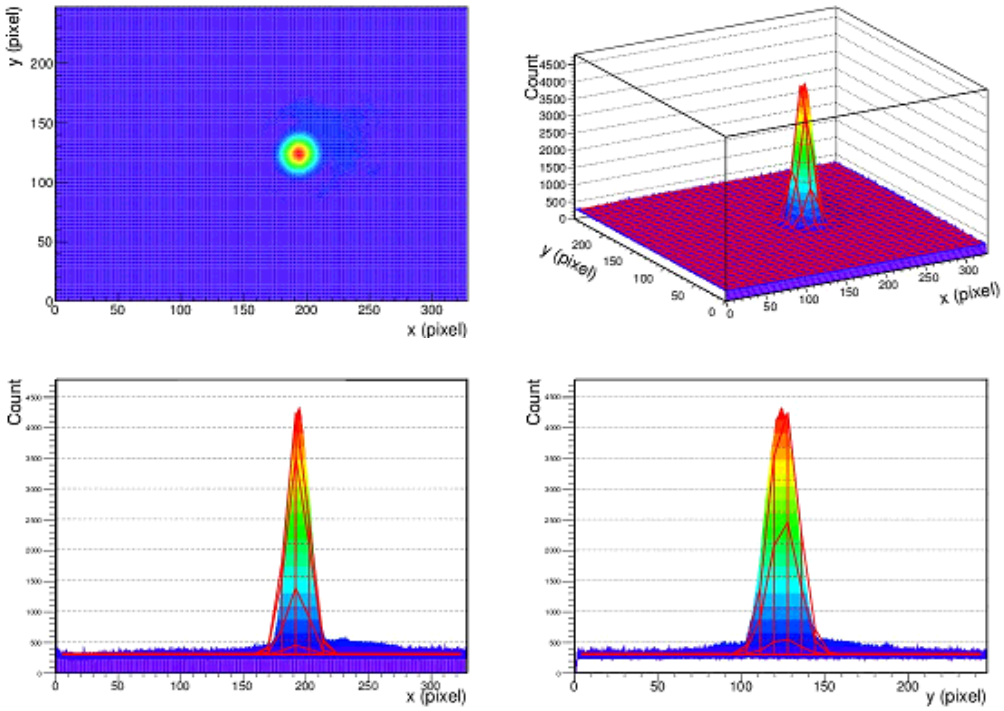

Figure 32. The beam profile of the creation laser at the focal spot

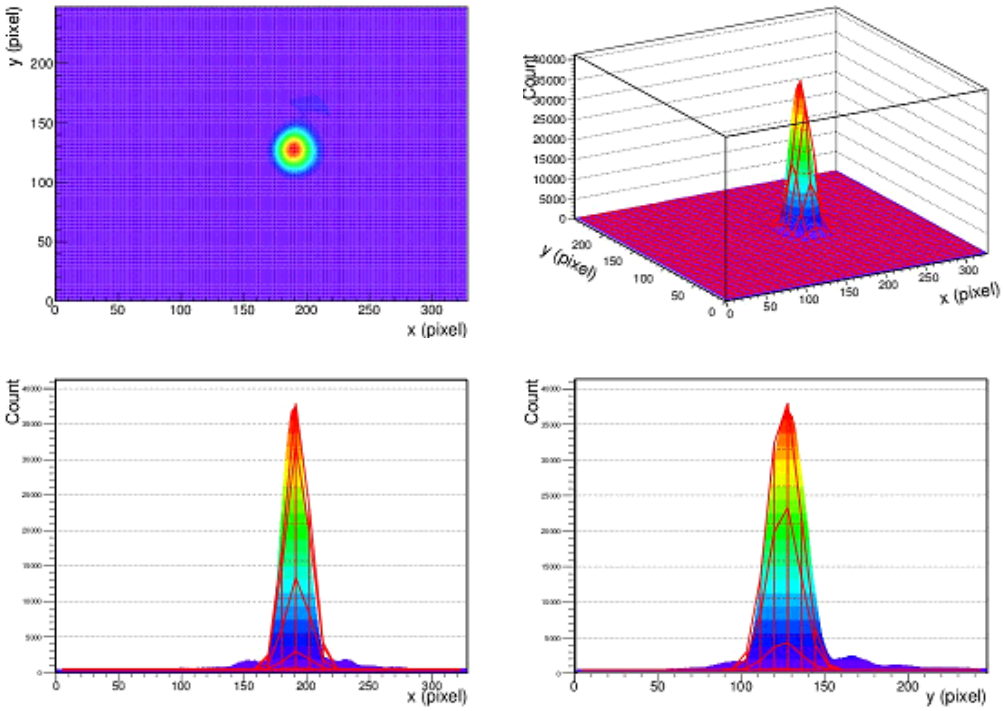

Figure 33. The beam profile of the inducing laser at the focal spot

5.3 Beam energies

The beam energies of the creation and inducing lasers are monitored by photo diodes PD1 and PD2, respectively.

The beam energy of the creation laser is calibrated by the charge sum of waveform data from PD1. The energy of the inducing laser is calibrated by the peak voltage of waveforms from PD2, because the charge sum is not sensitive to in the case of the inducing laser duo to its long time duration.

The beam energies are measured by a power meter at a backward of the beam aperture on each beam line. The waveforms of photo diodes and the beam energies measured by the power meter are recorded in parallel by changing the beam energies with inserting optical filters.

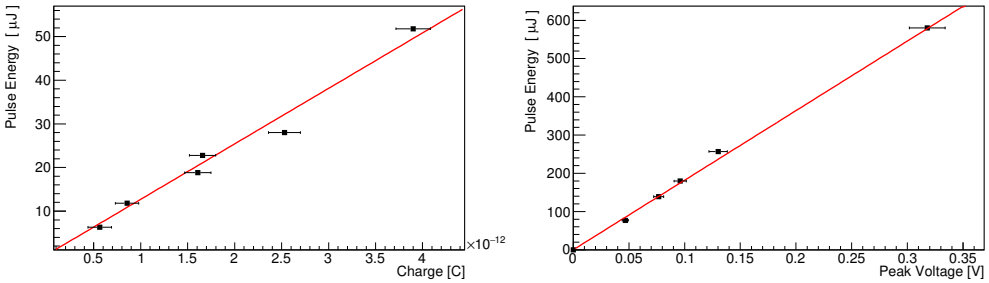

Figure 34. The correlation between the charge sum and the pulse energy of the creation laser is shown in the left panel. The correlation between the peak voltage and the pulse energy of the inducing laser is shown in the right panel. They are fitted by the linear functions drawn by the red lines.

The charge distribution of the creation laser and the peak voltage distribution of the inducing laser are shown at left and right panels in Fig. 35, respectively. The mean of the charge distribution of the creation laser is $5.31 \pm 0.78 \times 10^{-12}$ C and the mean of the peak voltage distribution of the inducing laser is -0.34 ± 0.01 V. The pulse energies at the sampling points are evaluate by extrapolate the mean values to the linear functions drawn in Fig. 34.

The pulse energies of the creation and inducing lasers at the sampling points are $E_c^* = 44.6 \pm 5.9$ μJ and $E_i^* = 617.4 \pm 3.5$ μJ, respectively.

However, the beam energies attenuate by propagating from the sampling points to the focal spot. The attenuation factors are evaluated by measuring the beam energies at the sampling points and the focal spot with the power meter after the physics run. The measured attenuation factor of the creation laser is $\kappa_c = 0.21$, and that of the inducing laser is $\kappa_c = 0.19$. The pulse

energies of the creation and inducing lasers at the focal spot E_c and E_i are evaluate as follows:

$$\begin{aligned} E_c &= \kappa_c E_c^* = 9.3 \pm 1.2\ \mu\text{J}, \\ E_i &= \kappa_i E_i^* = 117 \pm 1\ \mu\text{J}. \end{aligned} \tag{57}$$

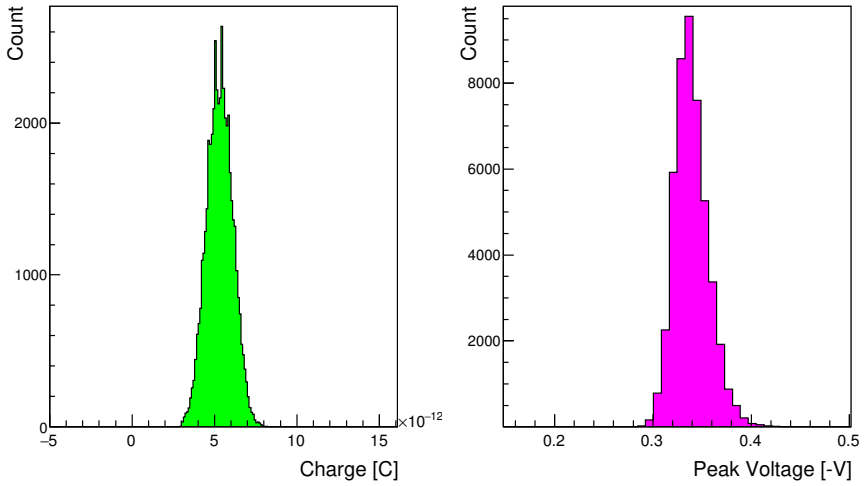

Figure 35. The charge distribution of the creation laser (left) and the peak voltage distribution of the inducing laser (right).

5.4 The pulse duration of the creation laser

The pulse duration of the creation laser τ_c is measured by using the autocorrelation method. Figure 36 illustrates the measurement setup. The creation laser are split by a beam splitter (BS). The two beams travel the different optical length and the split beams are combined by another BS again.

The combined pulse is composed of the two pulses which have a tiny amount of time difference due to their different optical lengths. The relative time delay between two pulses are adjustable by sliding the linear transition stage.

The combined beam enters a BBO (BaB_2O_4) crystal and converts into the second harmonic wave ($\lambda = 400$ nm). The intensity of the second harmonic wave depends on the number of time-coincidental photons in the combined pulse. Therefore, the time duration of the laser pulse are evaluated by measuring correlation between a time delay and the intensity of the second harmonic wave.

The intensity of the second harmonic wave are measured by the PMT. The optical filters transmit 380 - 430 nm wavelength photons are placed in front of the PMT. The pulse duration of the creation laser τ_c is evaluated as

$$\tau_c = \frac{\Delta\tau}{\alpha}, \tag{58}$$

where $\Delta\tau$ is the time duration of the autocorrelated signal shown in Fig.36, and α is the autocorrelation factor.

$\Delta\tau$ is defined as $\Delta\tau = 2\Delta L/c$, where $\Delta L = 0.2$ mm is the full width at half maximum of the fitting gauss function of the autocorrelated signal shown in Fig.37. The autocorrelation factor $\alpha = \sqrt{2}$ is assigned with the assumption that the time structures of the laser pulses follow the Gaussian distribution. From Eq.(58), the pulse duration of the creation laser τ_c is given as

$$\tau_c = 900 \text{ fm}. \tag{59}$$

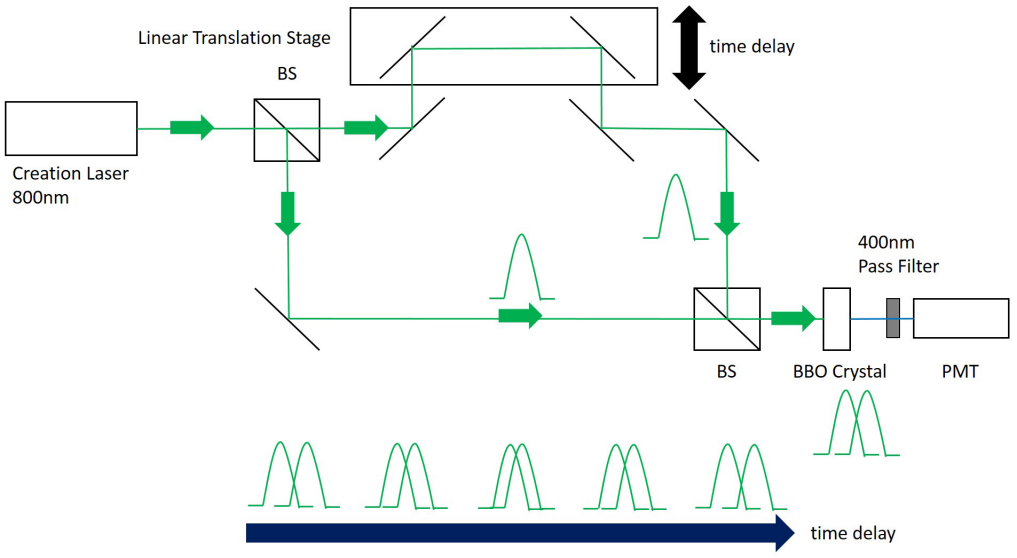

Figure 36. The setup to measure the pulse duration of the creation laser via the autocorrelation method.

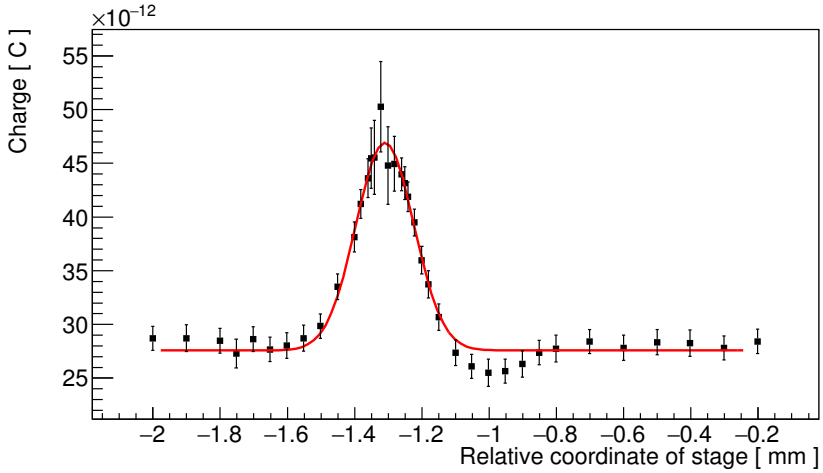

Figure 37. The intensity of the second harmonic wave depends on the relative coordination of the linear transformed stage.

5.5 The energy spectrum of the creation laser

The energy spectrum of the creation laser is measured in front of the focal spot by a spectrum analyzer. The measured wavelength distribution is shown in Fig.38. The effective spectrum width of the creation laser $\delta\omega_c$ is defined as

$$\delta\omega_c \text{ [eV]} = \frac{1}{2}\frac{hc}{e\delta\lambda_c}, \tag{60}$$

where h is the Planck constant, c is the velocity of light, e is the elementary charge. $\delta\lambda_c = 3$ nm is defined as the root mean square of the wavelength distribution shown in Fig.38. The spectrum width of the creation laser is evaluated from Eq.(60) as

$$\delta\omega_c \sim 0.005 \text{ eV} \tag{61}$$

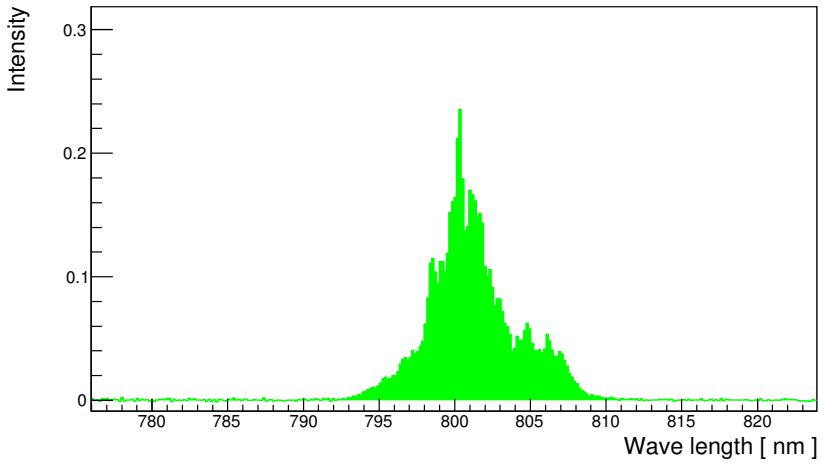

Figure 38. The wavelength spectrum of the creation laser.

5.6 Signal attenuation factor

The signal attenuation factor from the focal spot to the end of the long optical fiber, $\epsilon_{\rm opt2}$ is measured. This attenuation factor is composed of the transmittance of optical devices and the signal acceptance of the PMT.

The intensities of the {2}-polarized calibration light at in front of the vacuum chamber and at the PMT are measured in parallel. The calibration light are split by the BS and the energy at in front of the vacuum chamber is measured by a photo-multiplier-tube (PMT') which is the same model of the PMT used as the signal detector.

$\epsilon_{\rm opt2}$ is evaluate from following equation,

$$\epsilon_{\rm opt2} = \frac{N_{\rm PMT}}{N_{\rm PMT'}} R_{\rm att} R_{\epsilon_D}, \tag{62}$$

where $N_{\rm PMT}$ is the mean number of the incident photons per pulse measured at the signal detection point by PMT and $N_{\rm PMT'}$ is measured at in front of vacuum chamber by PMT', $R_{\rm att}$ is the attenuation factor from the sampling point to the focal spot, and R_{ϵ_D} is the ratio of detection efficiency of PMT and PMT'.

The measurement values of $N_{\rm PMT}$ and $N_{\rm PMT'}$ are

$$N_{\rm PMT} = 2.09 \pm 0.01, \tag{63}$$

$$N_{\rm PMT'} = (4.17 \pm 0.20) \times 10^2. \tag{64}$$

$R_{\rm att} = 0.26 \pm 0.06$ is measured at the sampling point and the focal spot by PMT' after physics run.

$R_{\epsilon_D} = 0.45 \pm 0.01$ is also measured when the detection efficiency of PMT is measured.

As a result, $\epsilon_{\rm opt2}$ is given as

$$\epsilon_{opt2} = 0.9 \pm 0.2\ \%. \tag{65}$$

5.7 Efficiency ratio between two optical fiber paths

$\epsilon_{\rm opt1}$, the signal attenuation factor for Path{1}, is evaluated from the ratio of path efficiencies B, where

$$B \equiv \frac{\epsilon_{\rm opt1}}{\epsilon_{\rm opt2}}. \tag{66}$$

B is measured by rotating the polarization angle Θ of the calibration light with the half wave plate, and counting the number of photons in $T\{1\}$ and $T\{2\}$.

The Θ dependences of the number of $\{1\}$ and $\{2\}$- polarized photons are plotted in Fig 39.

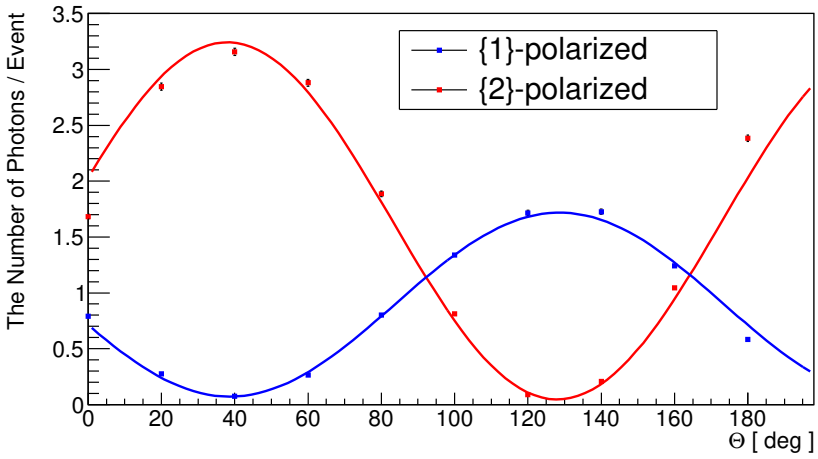

Figure 39. The number of $\{1\}$ and $\{2\}$-polarized photons as a function of the linear polarized angle Θ.

The data points for each polarization state are fitted by following function,

$$f(\Theta) = A(\cos 2\Theta + \phi) + C, \tag{67}$$

where A is the amplitude, ϕ is the phase, and C is the constant. B is re-expressed as $B = A_{\{1\}}/A_{\{2\}}$, where $A_{\{1\}}$ and $A_{\{2\}}$ are the amplitudes of the fitting functions of $\{1\}$ and $\{2\}$-polarized data, respectively. From Fig.39,

$$B = 0.51 \pm 0.01 \tag{68}$$

is given and

$$\epsilon_{\rm opt1} = B\epsilon_{\rm opt2} = 0.5 \pm 0.1\ \% \tag{69}$$

is obtained.

6 Results

6.1 Observed photon counts in vacuum

The physics run search for scalar and pseudoscalar fields was performed at 2.3×10^{-2} Pa. The time distributions of observed photons are shown in Fig.40.

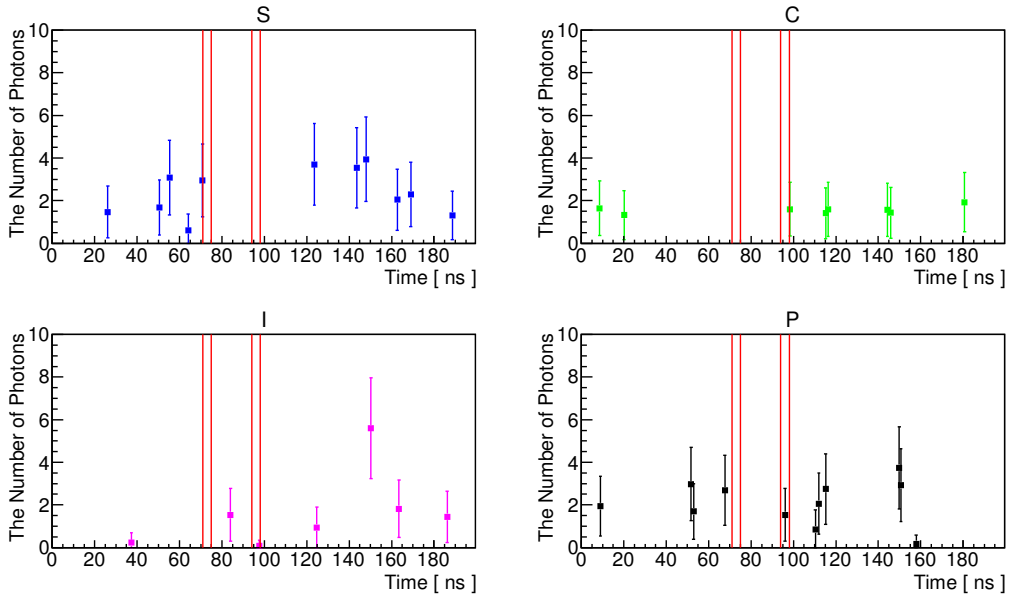

Figure 40. The time distributions of the observed photons (efficiency-uncorrected) at $2.3 \times 10^{-}2$ Pa [47]. The data points in each trigger pattern are normalized to the number of triggered events of S trigger pattern.

From Tab.2, it is confirmed that no four-wave mixing photon is observed in vacuum. Furthermore, residual photons in the creation and inducing lasers are also not observed at the detection point.

The number of the four-wave mixing photons are evaluated with following strategy. It is assumed that the number of observed photon n_i for each

Table 2: The numbers of observed photons in $T\{1\}$ and $T\{2\}$ for each trigger pattern. n_{i1} and n_{i2} are the number of signals in trigger pattern i with $\{1\}$ and $\{2\}$-polarized states, respectively. W_i is the number of events in trigger pattern i.

Trigger i	n_{i1}	n_{i2}	W_i
S	0	0	46120
C	0	0	46203
I	0	0.07	46044
P	0	1.53	46169

trigger pattern i are composed of following components

$$
\begin{aligned}
n_S &= N_P + N_C + N_I + N_S, && (70)\\
n_C &= N_P + N_C, && (71)\\
n_I &= N_P + N_I, && (72)\\
n_P &= N_P, && (73)
\end{aligned}
$$

with an assumption that the number of observed photons at P-pattern n_P is come from thermal noises from the PMT and ambient noises such as cosmic rays (N_P). All trigger patterns should contain N_P by considering the event weights of the four trigger patterns. N_C and N_I are come from the residual photons in the creation and inducing lasers, respectively. They furthermore contain the photons produced by nonlinear interactions at optical materials or gas when the creation or inducing laser is incident, individually. N_S is the number of signal photons originating from the four-wave mixing process. This should appear at S-pattern.

N_S is evaluate from Eq.(73), as follows:

$$
\begin{aligned}
N_S &= n_S - \frac{W_S}{W_P}n_P - \frac{W_S}{W_C}(n_C - n_P) - \frac{W_S}{W_I}(n_I - n_P)\\
&= n_S - \frac{W_S}{W_C}n_C - \frac{W_S}{W_I}n_I + \frac{W_S}{W_P}n_P. && (74)
\end{aligned}
$$

The time distribution of N_S is shown in Fig.41. It is obtained by subtractions among the time distributions of the four-trigger patterns shown in Fig.40 based on the relation in Eq.(74). Figure 41 indicates that no excess is shown in time domains $T\{1\}$ and $T\{2\}$. It means the four-wave mixing signals are not observed in this search.

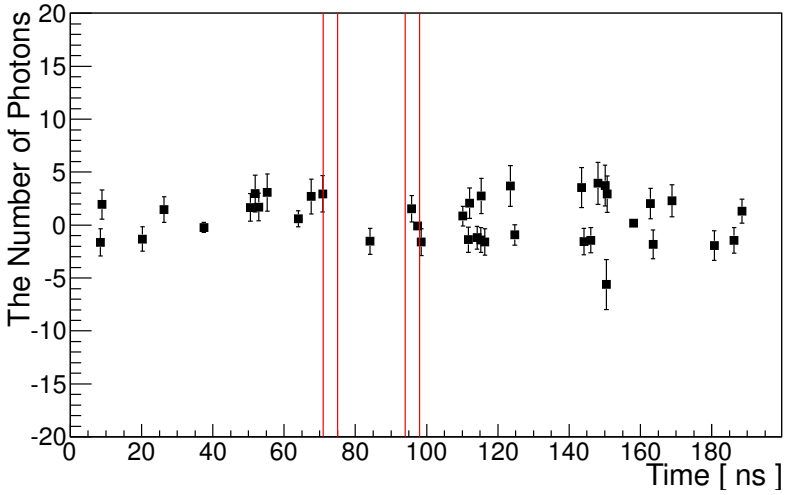

Figure 41. The time distribution of the number of signal photons N_S (efficiency-uncorrected) at 2.3×10^{-2} Pa.

As a result, the number of observed signal photons with {1} and {2}-polarized states are obtained as follows:

$$N_{S1} = \quad 0 \pm 0(\text{stat.}) \pm 2.16(\text{syst.I}) \pm 0.30(\text{syst.II}) \pm 0(\text{syst.III}),$$
$$N_{S2} = \quad 1.46 \pm 1.27(\text{stat.}) \pm 2.16(\text{syst.I}) \pm 0.04(\text{syst.II}) \pm 3.59(\text{syst.III}).$$

6.2 Systematic errors

Systematic error I is come from the number of the photons outside of the two arrival time domains $T\{1\}$ and $T\{2\}$. This is evaluated by calculating the root mean square of N_S except in $T\{1\}$ and $T\{2\}$.

Systematic error Ⅱ is originating from the ambiguity of the number of signals depends on the uncertainty of the threshold value $V_{\rm t}$ for the peak finding. It is estimated by changing $V_{\rm t}$ from -1.2 mV to -1.4 mV.

Systematic error Ⅲ is relevant to the ambiguities of the threshold value $n_{\rm node}$ for the rejection of noisy events shown in Fig.16.

The number of signals by changing $V_{\rm t}$ and $n_{\rm node}$ are listed in Tab.3. $V_{\rm t}$ and $n_{\rm node}$ are changed independently. When estimate syst.I, $n_{\rm node}$ is fixed to 150. In the case of syst.Ⅱ estimation, $V_{\rm t}$ is fixed to -1.3 mV.

Table 3: The data table of N_{S1} and N_{S2} depends on $V_{\rm t}$ and $n_{\rm node}$.

$V_{\rm t}$ [mV]	N_{S1}	N_{S2}	$n_{\rm node}$	N_{S1}	N_{S2}
-1.2	0.52	1.46	145	0	-4.75
-1.3	0	1.46	150	0	1.46
-1.4	0	1.53	155	0	1.46

It is assumed that uncertainties of N_{S1} and N_{S2} originating from the ambiguities of $V_{\rm t}$ and $n_{\rm node}$ are based on uniform distributions. Here syst.Ⅱ and syst.Ⅲ are defined as the standard deviation of uniform distributions.

7 Background Estimation

7.1 Four-wave mixing process in residual gas

The four-wave mixing photons can be emitted from the focal volume by interaction between high intensity lasers and residual gas into the vacuum chamber.

The four-wave mixing process by interacting with atoms is interpreted as the third-order nonlinear quantum optical process[41, 42]. It is considerable background source since it can be the main background component at higher intensity laser experiments in the future.

In this experiment, the expected number of the four-wave mixing photons from gas is estimated by measuring its pressure dependence. The number of the four-wave mixing photons in gas is evaluated with similar analysis method at the vacuum condition.

Figure 42 shows the pressure dependence of the number of the four-wave mixing photons. The black and red data points indicate {1} and {2}-polarized photons, respectively, and they are fitted by the quadratic functions.

The expected number of the four-wave mixing photons with the same shot statistics as the vacuum data at 2.3×10^{-2} Pa (an equivalent condition to the vacuum data) are estimated as

$$\begin{aligned} \mathcal{N}_{\mathrm{gas1}} &= 1.7 \pm 1.1 \times 10^{-5}, \\ \mathcal{N}_{\mathrm{gas2}} &= 1.7 \pm 1.1 \times 10^{-5}, \end{aligned} \tag{75}$$

where $\mathcal{N}_{\mathrm{gas1}}$ and $\mathcal{N}_{\mathrm{gas2}}$ are the number of {1} and {2}-polarized photons (efficiency-corrected), respectively. Thus the number of the four-wave mixing photons emitted from residual gas are negligible small in this search experiment.

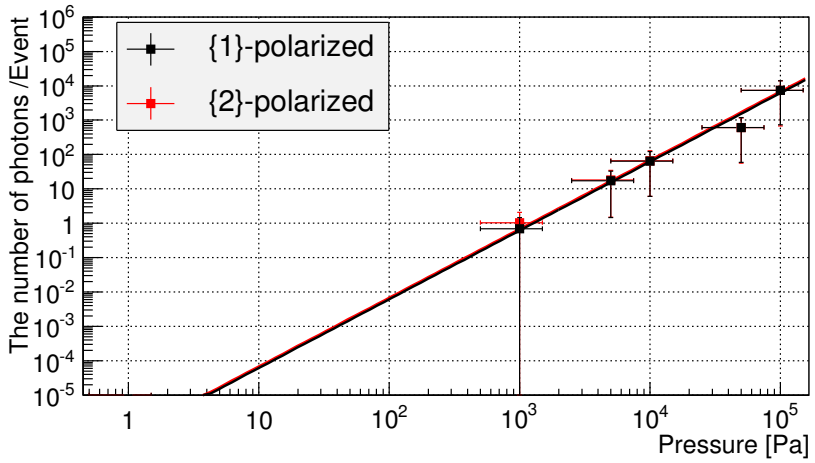

Figure 42. The pressure dependence of the number of four-wave mixing photons per pulse [47].

The correlations between the energies of the incident lasers and the number of the four-wave mixing photons in gas are also measured. The beam energies of the creation and inducing lasers are changed independently by inserting optical filters on each beam line. The energies of the creation and inducing lasers dependences are shown in Fig.43 and Fig.44, respectively.

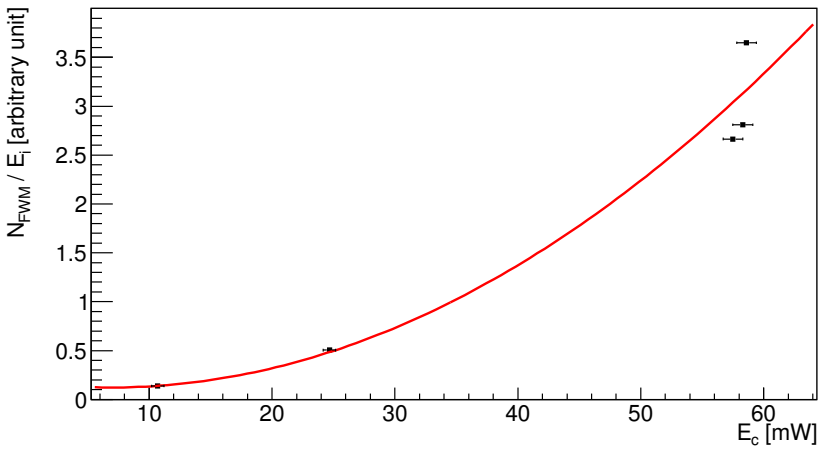

Figure 43. The correlations between the pulse energy of the creation laser E_c and the number of the four-wave mixing photons in gas N_{FWM} fitted by the quadratic function. The vertical axis is scaled by E_i and the numerical values are notated in arbitrary unit.

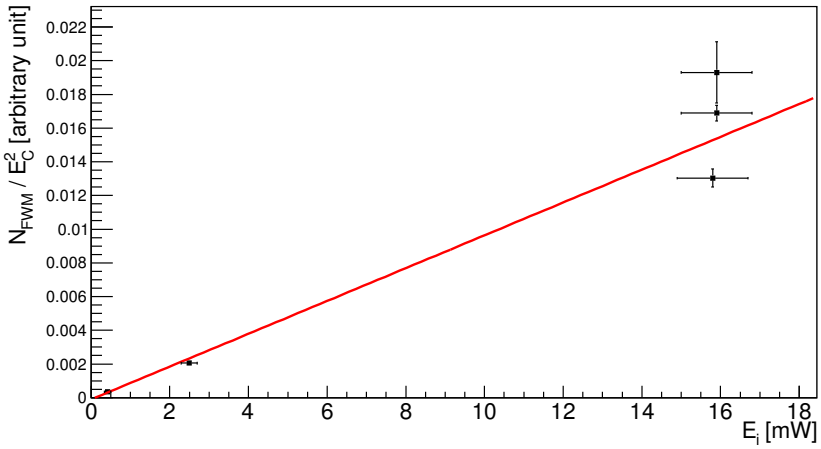

Figure 44. The correlations between the pulse energy of the inducing laser E_i and N_{FWM} fitted by the linear function. The vertical axis is scaled by E_c and the numerical values are notated in arbitrary unit.

In addition, the number of the four-wave mixing photons N_{FWM} divided by ${E_c}^2 E_i$ at the different beam energies conditions are plotted in Fig.45. They become constant among the different beam energies conditions. It agrees with the intensity dependence of the four-wave mixing photons $I_4 \propto {I_1}^2 I_2$ shown in Eq.(35).

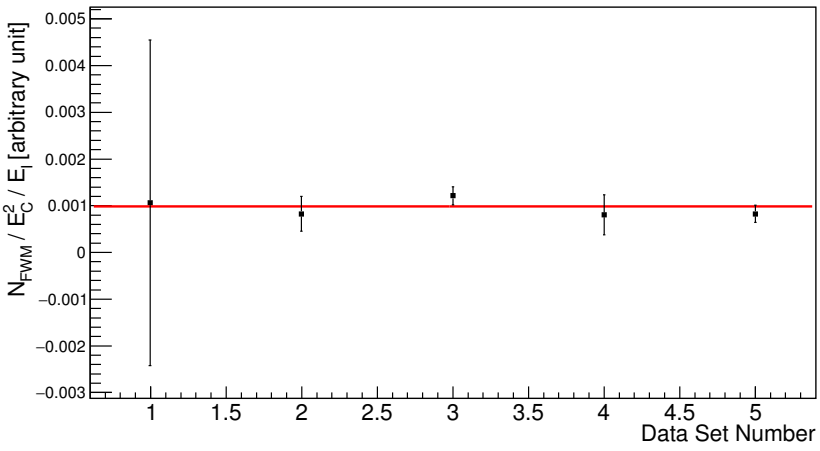

Figure 45. $N_{\mathrm{FWM}}/E_c^2/E_i$ at the different beam energies conditions fitted by constant.

7.2 Photon-photon scattering by nonlinear QED effect

The QED (Quantum Electro Dynamics) predicts photon-photon interaction by the contribution of the electron loop originating from the nonlinear quantum effect of vacuum (Fig.46). The background photons can be produced via this process in QPS. The cross section of photon-photon scattering in the QED process is expressed as

$$\sigma_{\mathrm{QED}} = \frac{973}{10125\pi}\alpha^2\gamma_e^2\left(\frac{\hbar\omega_{\mathrm{cms}}}{m_e c^2}\right), \tag{76}$$

where $\alpha \sim 1/137$ is the fine-structure constant, $\gamma_e \sim 2.8 \times 10^{-13}$ cm is the classical electron radius, ω_{cms} is the photon energy in the center-of-mass system, and $m_e \sim 0.5$ MeV is the electron mass .

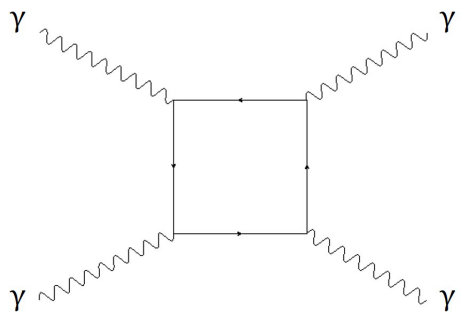

Figure 46. The Feynman diagram of the photon-photon scattering via nonlinear QED process.

We now roughly estimate the order of σ_{QED} with $\omega = 0.1$ eV,

$$\sigma_{\mathrm{QED}} \sim 10^{-75}\ \mathrm{m}^2. \tag{77}$$

The luminosity L of the photon-photon scattering in QPS including the inducing photons per shot are expressed simply as

$$L = \frac{N_c^2 N_i}{2\pi W_0^2}\sin\Delta\vartheta^2, \tag{78}$$

where $N_c \sim 10^{14}$ and $N_i \sim 10^{15}$ are the number of photons in the pulse of the creation and inducing lasers, respectively, $W_0 \sim 10\ \mu$m is the focal spot radius, and $\Delta\vartheta \equiv d/2f \sim 0.1$.

L is evaluated as

$$L \sim 10^{47}\ \mathrm{m}^{-2}. \tag{79}$$

The number of the photon-photon scattering processes expected with whole shot statistics in this experiment are expressed as

$$\mathcal{N}_{\mathrm{QED}} = \sigma_{\mathrm{QED}} L W_S, \tag{80}$$

where $W_S \sim 50000$ is the number of S-triggered events.
N_{QED} is roughly estimated as

$$N_{\mathrm{QED}} \sim 10^{-23}. \tag{81}$$

We note that these calculation overestimates the scattering rate, since we now assume that all inducing photons contribute to the inducing effect. A rigorous derivation of the photon-photon scattering rate by the QED process in the QPS geometry can be evaluated by taking the phase matching between the creation and inducing photons into account. We overestimate the scattering rate, nevertheless, it is negligible small in this experimental condition. Therefore, the background signals originating from the nonlinear QED process are no less negligible in this experiment.

8 Exclusion limits for scalar and pseudoscalar fields

8.1 Coupling - mass relations

The coupling-mass relations of scalar and pseudoscalar fields are evaluated from Eq.(31). The efficiency-corrected number of {1}-polarized photons $\mathcal{N}_{S1}$ and that of {2}-polarized photons $\mathcal{N}_{S2}$ are evaluated with the experiment parameters as

$$\mathcal{N}_{S1} = \frac{N_{S1}}{\epsilon_{\rm opt1}\epsilon_D}, \quad \mathcal{N}_{S2} = \frac{N_{S2}}{\epsilon_{\rm opt2}\epsilon_D}. \tag{82}$$

The upper limits of the signal yields per shot in the case of scalar and pseudo scalar fields exchange at a 95% confidence level are evaluated as

$$\mathcal{Y}_{\rm sc} = \frac{2.24\delta N_{S2}}{\epsilon_{\rm opt2}\epsilon_D W_S}, \quad \mathcal{Y}_{\rm ps} = \frac{2.24\delta N_{S1}}{\epsilon_{\rm opt1}\epsilon_D W_S}, \tag{83}$$

respectively.

We now assume the true number of signal yield is 0, since no significant signal is observed and the expected number of backgrounds are negligible. Therefore, the number of observed signals should follows the Poisson distribution whose mean is 0. δN_{S1} and δN_{S2} are defined as the standard deviations of the Poisson distributions and they are evaluated from the quadratic sum of the statistical and systematic errors of N_{S1} and N_{S2}, respectively. The upper limits of the searched mass ranges of both fields are given as

$$m < 2\omega \sin\Delta\theta \sim 2\omega\frac{d}{2f} = 0.15 \text{ eV}. \tag{84}$$

The exclusion limits for scalar and pseudoscalar fields obtained from this experiment are shown in Fig.47 and Fig.48, respectively.

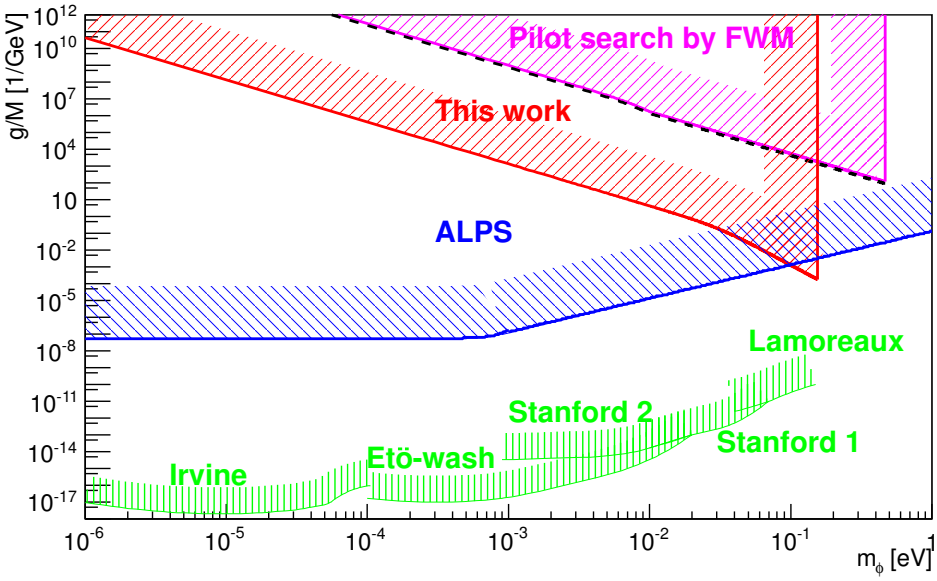

Figure 47. Exclusion limits for scalar fields (ϕ) in ϕ-photon coupling (g/M) as a function of mass of ϕ (m_ϕ) [47]. The excluded region at a 95% confidence level obtained from this experiment is drawn by the red shaded area. The magenta shaded area shows the excluded region by previous search in QPS [48], which is renewed from the black dotted line obtained from Ref.[48] by taking the incident-plane-rotation factor $\mathcal{G}$ into account. The blue shaded area represents the excluded region for scalar fields by light shining through a wall experiment "ALPS" [32] (the sine function part of the sensitivity curve is simplified to unity for drawing purposes at the mass region above 10^{-3}eV,). The green shaded areas indicate the limits given by non-Newtonian force searches by torsion balance experiments "Irvine" [49], "Eto-wash" [50, 51], "Stanford1" [11], "Stanford2" [8] and Casimir force measurement "Lamoreaux"[9].

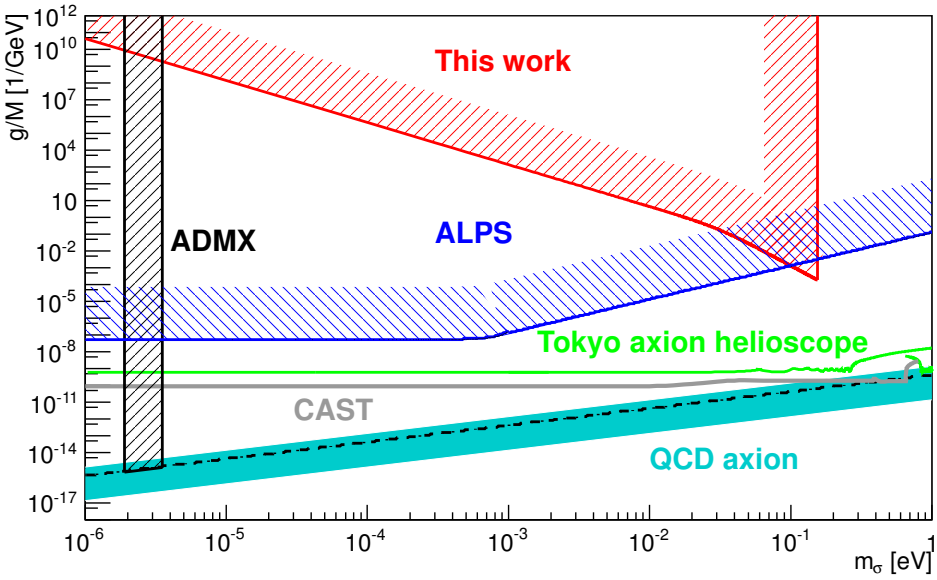

Figure 48. Exclusion limits for pseudoscalar fields (σ) in σ-photon coupling (g/M) as a function of mass of σ (m_σ) [47]. The blue shaded area shows the excluded region by the pseudoscalar search, "ALPS". The green and gray solid line show the exclusion limits from the solar axion experiments "Tokyo Axion Helioscope" [21, 22, 23] and "CAST" [25, 26, 27] , respectively. The black shaded area represents the result from the dark matter axion search using a microwave cavity "ADMX" [33, 34]. The cyan band indicates the expected coupling-mass relation of QCD axion predicted by KSVZ model[36, 37] with $|E/N - 1.95|$ in the range 0.07-7, furthermore, in the case of $E/N = 0$ is shown by the black dotted line.

8.2 Data table of experimental parameters

The experimental parameters are summarized in Tab.4. $\mathcal{G}^{\rm sc}$ and $\mathcal{G}^{\rm ps}$ represent $\mathcal{G}$ in the case of scalar and pseudoscalar fields exchange, respectively. The evaluation of $\mathcal{G}$ is discussed in Appendix A of this thesis.

$\mathcal{F}^{\rm sc}_{1122}$ and $\mathcal{F}^{\rm ps}_{1212}$ denote $\mathcal{F}_S$ in the case of scalar and pseudoscalar fields exchange, respectively. See the detail in Appendix B of this thesis.

The center of the wavelength of the inducing laser λ_i, the line width of the inducing laser $\delta\omega_4$, and the pulse duration of the inducing laser τ_i are referred from the values published by Spectra Physics.

The energy of the inducing laser per τ_i is evaluated as $E_i = \eta E_i^*$, where $\eta = 0.87$ is the overlapping factor given from section 5.2, and $E_i^* = 117.4 \pm 0.7$ μJ is obtained from Eq.(57).

The single-photon detection efficiency at 641nm is evaluated as $\epsilon_D = \xi \epsilon_D^*$, where $\xi = 0.67$ is the relative quantum efficiency between 532nm and 641nm lights provided by HAMAMATSU, and $\epsilon_D^* = 2.4 \pm 0.1$ % is given from Eq.(49).

Table 4: Data table of experimental parameters.

Parameters	Values
Center of wavelength of creation laser λ_c	800 nm
Relative line width of creation laser $(\delta\omega/\langle\omega\rangle)$	3.8×10^{-3}
Center of wavelength of inducing laser λ_i	1064 nm
Relative line width of inducing laser $(\delta\omega_4/\langle\omega_4\rangle)$	5.0×10^{-5}
Duration time of creation laser pulse per injection τ_c	900 fs
Duration time of inducing laser pulse per injection τ_i	9 ns
Creation laser energy per τ_c	9.3 ± 1.2 μJ
Inducing laser energy per τ_i	100 ± 1 μJ
Focal length f	200 mm
Beam diameter of laser beams d	20 mm
Upper mass range given by $\theta < \Delta\theta$	0.15 eV
$u = \omega_4/\omega$	0.75
Incident plane rotation factor $\mathcal{G}$	$\mathcal{G}_{11}^{\mathrm{sc}}$=19/32
	$\mathcal{G}_{12}^{\mathrm{ps}}$=1/2
Axially asysmmetric factor $\mathcal{F}_S$	$\mathcal{F}_{1122}^{\mathrm{sc}}$=19.4
	$\mathcal{F}_{1212}^{\mathrm{ps}}$=19.2
Combinatorial factor in luminosity C_{mb}	1/2
Single-photon detection efficiency at 641nm ϵ_D	1.4 ± 0.1 %
Efficiency of optical path from interaction point to path{1} ϵ_{opt1}	0.5 ± 0.1 %
Efficiency of optical path from interaction point to path{2} ϵ_{opt2}	0.9 ± 0.2 %
δN_{S1}	2.2
δN_{S2}	4.4

9 Conclusion

The search for scalar and psudoscalar fields via the quasi parallel colliding system (QPS) was performed by combining a 9.3 μJ/0.9 ps Ti-Sapphire laser and a 100 μJ/9 ns Nd:YAG laser at 2.3×10^{-2} Pa.

The number of {1} and {2}-polarized signal-like photons are $N_{S1} = 0 \pm 0(\text{stat.}) \pm 2.16(\text{syst.I}) \pm 0.30(\text{syst.II}) \pm 0(\text{syst.III})$ and $N_{S2} = 1.46 \pm 1.27(\text{stat.}) \pm 2.16(\text{syst.I}) \pm 0.04(\text{syst.II}) \pm 3.59(\text{syst.III})$, respectively.

As a result, no significant signal was observed and the exclusion limits for scalar and psudoscalar fields were obtained at a 95% confidence level below 0.15 eV mass range. The most sensitive coupling limits $g/M = 2.05 \times 10^{-4}$ GeV^{-1} for scalar search and $g/M = 2.12 \times 10^{-4}$ GeV^{-1} for pseudoscalar search are obtained at $m = 0.15$ eV.

The pressure dependences of the four-wave mixing photons emitted from residual gas in the vacuum chamber were measured. The expected number of {1} and {2}-polarized photons are $\mathcal{N}_{\text{gas1}} = 1.7 \pm 1.1 \times 10^{-5}$, and $\mathcal{N}_{\text{gas2}} = 1.7 \pm 1.1 \times 10^{-5}$ at 2.3×10^{-2} Pa.

The experimental methods developed in this thesis can be applicable to the future experiments with higher intensity lasers.

10 Future prospects

Here prospects for the future experiments with higher intensity lasers are discussed. There are several issues which can be considerable in the conditions using higher intensity lasers.

- How to suppress the number of background signals and how to estimate the number of them?

  The four-wave mixing photons from gas are negligible in this experiment. However, the finite number of background signals can be observed in higher intensity laser fields. They can be suppressed by achieving a higher vacuum pressure since the background signals have the quadratic dependence of the pressure as shown in Fig.42.

  If we use 1PW (10^{15} W) lasers in the future experiments, the vacuum pressure 10^{-10} Pa are necessary to suppress the four-wave mixing photon in gas less than 1 photon per shot. Achieving 10^{10}Pa is not easy since a large volume of vacuum components, for example, a vacuum chamber and beam transporting pipes, are used in high intensity laser systems. The reasonable solution is introducing the differential pumping system near the focal spot.

  In the high vacuum pressure, the quadratic pressure dependence of background signals can no be assured since the partial pressure should no be similar to that of near an atmospheric pressure. Therefore, the number of background signals should be estimated by considering what atoms dominate the measured pressure, and how many background photons expected to be emitted from them.

  Furthermore, the four-wave mixing photons emitted from optical components are also considerable. The material which through the intense laser can be main background sources. Thus, they should not be placed before signals are separated from incident lasers. For example, beam focusing should be done by not a convex lens but a parabolic mirror.

- How much sensitivity can future experiments reach?

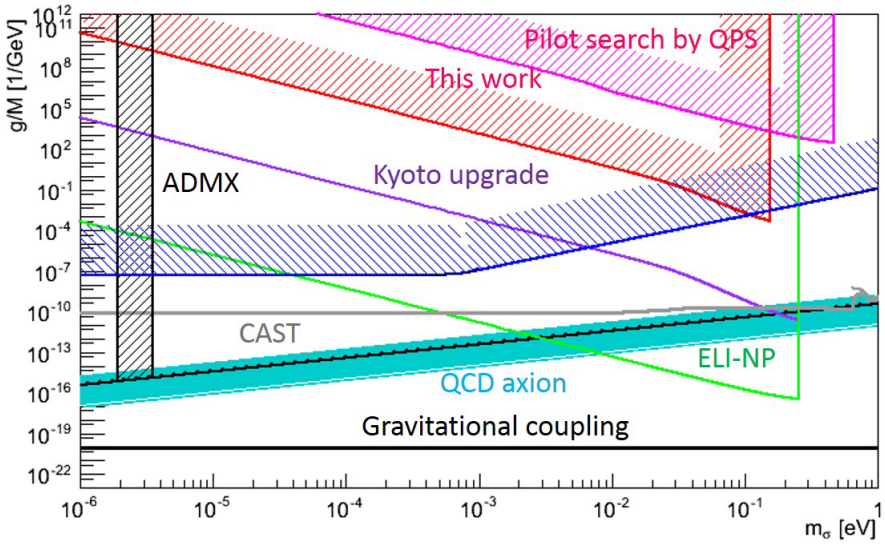

Figure 49. The expected sensitivities obtained by future experiments.

An upgraded experiment is developing with 10TW laser at Kyoto university and 10PW laser at ELI-NP (Extreme Light Infrastructure - Nuclear Physics) [52], which is being constructed in Romania and it will run from 2018. The expected sensitivities are shown in Fig.49. The purple line is expected sensitivity by Kyoto 10TW experiment and it will reach to QCD axion line at sub-eV mass region. The green line indicates the expected sensitivity in ELI-NP. The sensitivity by ELI-NP experiment will not reach to the gravitational coupling. Therefore, extremely higher intensity lasers are required for the dilaton search.

Here the worldwide laser community IZEST (International center on Zette-Exawatt Science and Technology) [53] is introduced. This is associated from more than 30 institutions including Kyoto university and ELI-NP to develop the extremely high intensity lasers and contributing to fundamental physics research. The dark field search experiment via QPS is positioned as one of the important researches in IZEST community. Therefore, the dilaton search will become factual in the future.

Acknowledgement

First of all, I express my gratitude to Assist. Prof. K. Homma. for giving me the opportunity for studying this exciting subject. Enormous amount of time for discussion with him guide my doctoral thesis to complete.

I gratefully thank my supervisor Prof. T. Sugitate for his general support and advice for my academic life.

I cordially appreciate Prof. S. Sakabe for his much support and tutelage for my research in Kyoto University. I express my gratitude to Assoc. Prof. M. Hashida, Assist. Prof. S. Inoue, Assist. Prof. S. Tokita, Dr. K. Otani and Dr. Y. Miyasaka for giving me a lot of advice about the experimental knowledges and techniques about laser optics. They always provided high quality experimental environment to me during my stay in Kyoto University.

K. Kume contributes a lot to develop the analysis method and the experimental setup at the early phase of this experimental research.

I acknowledge Y. Inoue providing the data list of the sensitive curve for the Tokyo axion helioscope.

I appreciate T. Takahashi for his appropriate advice and discussion for my doctoral thesis.

I gratefully thank all members of quark physics laboratory at Hiroshima University and members of Sakabe laboratory in Kyoto University.

Finally, I would like to thank my parents for their long-term support during my academic life.

Appendix A: Incident plane rotation factor $\mathcal{G}$

The relations of the linear polarization states between the initial and final state photons can be written as

$$\begin{aligned} \omega\{1\} + \omega\{1\} &= \omega_3\{1\} + \omega_4\{1\}, \\ \omega\{1\} + \omega\{1\} &= \omega_3\{2\} + \omega_4\{2\}, \end{aligned} \tag{85}$$

or

$$\begin{aligned} \omega\{1\} + \omega\{2\} &= \omega_3\{1\} + \omega_4\{2\}, \\ \omega\{1\} + \omega\{2\} &= \omega_3\{2\} + \omega_4\{1\}. \end{aligned} \tag{86}$$

Equations(85) and (86) correspond to the case of scalar and pseudoscalar fields exchange, respectively. We note that these descriptions can be applied when all photons are on the same reaction plane. However, in the focused geometry in QPS, the theoretical incident polarization plane consists of the incident photon pair p_1 and p_2 has a rotational degree of freedom. Therefore, if we fix the polarization vector of the incident laser to $\{1\}$ or $\{2\}$, the theoretical polarization vectors (1) and (2) are defined independently. As a result, the focusing QPS has the sensitivity for scalar and pseudoscalar fields, simultaneously, even we fix the polarization vectors of the incident photons to $\{1\}$ or $\{2\}$.

The outgoing $p_3 - p_4$ plane also has the rotation degree of freedom with the rotation angle φ independent of the rotation of the incident $p_1 - p_2$ plane.

To evaluate the signal yields of scalar and pseudoscalar fields in the focused QPS, a weighted averaging factor $\mathcal{G}$ over the rotation angle of the incident plane Φ is introduced.

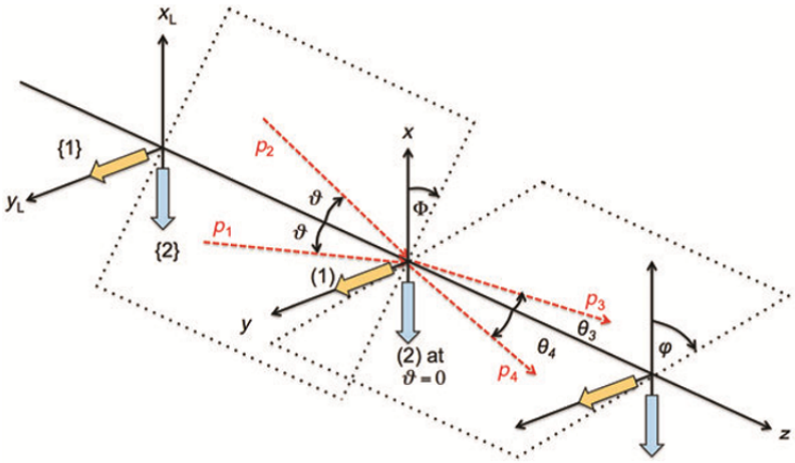

Figure 50. The definitions of polarization vectors and rotation angles in QPS [47].

First of all, the s-channel scattering amplitude is expressed as

$$\mathcal{M}_S = -(gM^{-1})^2 \frac{\mathcal{V}_{ab}^{[1]} \mathcal{V}_{cd}^{[2]}}{(p_1+p_2)^2+m^2}, \tag{87}$$

where $S \equiv$ abcd with a,b,c,d = 1 or 2, respectively, denotes a sequence of polarization states of four photons.

The Φ-dependent squared transition amplitude should be averaged over the possible rotation angle from 0 to 2π. Thus, we define the incident plane rotation factor as follows:

$$\mathcal{G}_{ab} \equiv \frac{\int_0^{2\pi} |\mathcal{V}_{ab}^{[1]}(\Phi)|^2 d\Phi}{\int_0^{2\pi} |\mathcal{V}_{ab}^{[1]}(\Phi=0)|^2 d\Phi}. \tag{88}$$

The vertex factors for the scalar fields exchange (SC) are expressed as

$$\begin{aligned} \mathcal{V}_{ab}^{[1]\mathrm{SC}} &= (p_1 p_2)(e_1^{(a)} e_2^{(b)}) - (p_1 e_2^{(a)})(p_2 e_1^{(b)}), \\ \mathcal{V}_{cd}^{[2]\mathrm{SC}} &= (p_3 p_4)(e_3^{(c)} e_4^{(d)}) - (p_3 e_4^{(c)})(p_4 e_3^{(d)}). \end{aligned} \tag{89}$$

In the pseudoscalar fields exchange (PS),

$$\mathcal{V}_{ab}^{[1]\mathrm{PS}} = -\epsilon^{\mu\nu\rho\sigma} p_{1\mu} p_{2\rho} e_{1\nu}{}^{(a)} e_{2\sigma}{}^{(b)}, \tag{90}$$

$$\mathcal{V}_{cd}^{[2]\mathrm{PS}} = -\epsilon^{\mu\nu\rho\sigma} p_{3\mu} p_{4\rho} e_{3\nu}{}^{(c)} e_{4\sigma}{}^{(d)}, \tag{91}$$

where ϵ is the Levi-Civita tensor.

The momenta and polarization vectors of four photons are expressed as follows:

$$\begin{aligned}
e_i^{(1)} &= (0,1,0), \\
e_1^{(2)} &= (-\cos\vartheta, 0, \sin\vartheta), \\
e_2^{(2)} &= (-\cos\vartheta, 0, -\sin\vartheta), \\
e_3^{(2)} &= (-\cos\theta_3, 0, \sin\theta_3), \\
e_4^{(2)} &= (-\cos\theta_4, 0, -\sin\theta_4), \\
p_1 &= (\omega\sin\vartheta\cos\Phi, -\omega\sin\vartheta\sin\Phi, \omega\cos\vartheta), \\
p_2 &= (-\omega\sin\vartheta\cos\Phi, \omega\sin\vartheta\sin\Phi, \omega\cos\vartheta), \\
p_3 &= (\omega_3\sin\theta_3\cos\varphi, -\omega_3\sin\theta_3\sin\varphi, \omega_3\cos\theta_3), \\
p_4 &= (-\omega_4\sin\theta_4\cos\varphi, \omega_4\sin\theta_4\sin\varphi, \omega_4\cos\theta_4). \qquad (92)
\end{aligned}$$

We evaluate the first vertex factor in case of $ab = 11$ for the scalar exchange as

$$\begin{aligned}
\mathcal{V}_{11}^{[1]\mathrm{SC}} &= (p_1p_2)(e_1^{(1)}e_2^{(1)}) - (p_1e_2^{(1)})(p_2e_1^{(1)}) \\
&= \omega^2(\cos 2\vartheta - 1 + \sin^2(\vartheta)\sin^2\Phi) \sim \omega^2\vartheta^2(2 - \sin^2\Phi), \qquad (93)
\end{aligned}$$

where the approximation is based on $\vartheta \sim \vartheta_r \ll 1$.

In the case of $ab = 12$ for the pseudoscalar exchange,

$$\begin{aligned}
\mathcal{V}_{12}^{[1]\mathrm{PS}} &= -\epsilon^{\mu\nu\rho\sigma}p_{1\mu}p_{2\rho}e_{1\nu}{}^{(1)}e_{2\sigma}{}^{(2)} \\
&= -2\omega^2\sin^2\vartheta\cos\Phi. \qquad (94)
\end{aligned}$$

We obtain the incident plane rotation factor in case of the scalar exchange as

$$\mathcal{G}_{11}^{\mathrm{SC}} = \frac{\int_0^{2\pi}(2-\sin^2\Phi)^2 d\Phi}{8\pi} = \frac{19}{32}. \qquad (95)$$

In the case of the pseudoscalar exchange, we obtain

$$\mathcal{G}_{12}^{\mathrm{PS}} = \frac{\int_0^{2\pi}(\cos^2\varphi) d\varphi}{8\pi} = \frac{1}{2}. \qquad (96)$$

Appendix B: Axially asymmetric factor $\mathcal{F}_S$

The outgoing $p_3 - p_4$ plane has the rotation degree of freedom as well as the incident $p_1 - p_2$ plane. From Eq.(89), the second vertex factor in case of $cd = 22$ for the scalar exchange is given as

$$\begin{aligned}
\mathcal{V}_{22}^{[2]\mathrm{SC}} &= (p_3 p_4)(e_3^{(2)} e_4^{(2)}) - (p_3 e_4^{(2)})(p_4 e_3^{(2)}) \\
&= \omega_3\omega_4\{\cos(\theta_3+\theta_4)(\cos(\theta_3+\theta_4)-1) + (1+\cos^2\varphi)\sin\theta_3\sin\theta_4\cos\theta_3\cos\theta_3 \\
&+ (\sin^2\theta_3\cos^2\theta_4 + \sin^2\theta_4\cos^2\theta_3)\cos\varphi\}. \qquad (97)
\end{aligned}$$

For a small ϑ, the approximations $\sin\vartheta_3 \sim \sqrt{\mathcal{R}}\vartheta$ and $\sin\vartheta_4 \sim 1/\sqrt{\mathcal{R}}\vartheta$ are used with $\mathcal{R} \equiv \sin\theta_3/\sin\theta_4 = \omega_4/\omega_3$.

Then, $\cos(\theta_3+\theta_4)$ is rewritten as

$$\cos(\theta_3+\theta_4) \sim 1 - \vartheta^2(1+\hat{\mathcal{R}}), \qquad (98)$$

with

$$\hat{\mathcal{R}} \equiv \frac{1}{2}(\mathcal{R} + \mathcal{R}^{-1}). \qquad (99)$$

Equation (97) is approximated as

$$\mathcal{V}_{22}^{[2]\mathrm{SC}} \sim \omega_3\omega_4\vartheta^2\{\cos^2\varphi + (2\cos\varphi - 1)\hat{\mathcal{R}}\} \equiv \omega_3\omega_4\vartheta^2 F(\vartheta). \qquad (100)$$

The axially asymmetric factor $\mathcal{F}_S$ for the scalar exchange case are defined as

$$\mathcal{F}_{1122}^{\mathrm{SC}} \equiv \int_0^{2\pi} F^2(\varphi)d\varphi \sim 2\pi\left(\frac{3}{8} + 3\hat{\mathcal{R}}^2 - \hat{\mathcal{R}}\right). \qquad (101)$$

In the case of pseudoscalar exchange, the second vertex factor at $cd = 12$ are evaluated as

$$\begin{aligned}
\mathcal{V}_{12}^{[2]\mathrm{PS}} &= -\epsilon^{\mu\nu\rho\sigma} p_{3\mu} p_{4\rho} e_{3\nu}{}^{(1)} e_{4\sigma}{}^{(2)} \\
&= -\omega_3\omega_4\{\cos\theta_4(-\cos\theta_3 + \cos\theta_4) + \sin\theta_4(\sin\theta_4 + \sin\theta_3\cos\varphi) \\
&\sim -\omega_3^2\omega_4^2\vartheta^2\{\check{\mathcal{R}} + (\mathcal{R}^{-1}+1)\cos\varphi\} \equiv -\omega_3^2\omega_4^2\vartheta^2 G(\varphi), \qquad (102)
\end{aligned}$$

with

$$\check{\mathcal{R}} \equiv \frac{1}{2}(\mathcal{R} - \mathcal{R}^{-1}). \qquad (103)$$

As a result, the axially asymmetric factor for the pseudoscalar exchange is given as

$$\mathcal{F}_{1122}^{\mathrm{PS}} \equiv \int_0^{2\pi} G^2(\varphi) d\varphi \sim 2\pi \left(\check{\mathcal{R}} + \frac{1}{2} (\mathcal{R}^{-1} + 1)^2 \right). \tag{104}$$

Appendix C: The effect of finite spectrum widths of the creation and the inducing lasers

The description of the $\gamma\gamma \to \phi/\sigma \to \gamma\gamma$ process in QPS is based on the condition that the incident photon pair has the same photon energy ω and the same incident angle ϑ. However, the incident photons have the energy uncertainties due to the finite spectrum width of the creation laser. Therefore, the energy-asymmetric collisions of the incident photon pairs should be considered when evaluate the signal yield.

Here the energy conservation is introduced again.

$$\begin{aligned} \omega &+ \omega \to (2-u)\omega + u\omega \\ = \omega &+ \omega \to \omega_3 + \omega_4 \end{aligned} \tag{105}$$

The finite spectrum widths of the creation and inducing lasers give the uncertainty of u as $\underline{u} \leq u \leq \overline{u}$. As a result, the signal photon also has the finite spectrum width.

We now introduce the following notations for the photon energies as

$$\begin{aligned} \omega &= \langle\omega\rangle \pm \delta\omega \\ \omega_3 &= \langle\omega_3\rangle \pm \delta\omega_3 \\ \omega_4 &= \langle\omega_4\rangle \pm \delta\omega_4 \end{aligned} \tag{106}$$

where $\langle\omega\rangle$, $\langle\omega_3\rangle$, and $\langle\omega_4\rangle$ are the average of the energies of the creation, signal, and inducing photons, respectively, and $\delta\omega$, $\delta\omega_3$, and $\delta\omega_4$ are their energy fluctuations. $\delta\omega$ and $\delta\omega_4$ are given by the spectrum width of the creation and inducing lasers, respectively. These notations are based on the practical laboratory frame, referred to as L-system, with different incident photon energies ω_1 and ω_2 and corresponding incident angles ϑ_1 and ϑ_2. To apply the ideal description that the incident photon pair has the same incident photon energy and incident angle, referred to as $\langle L\rangle$-system, the following notations are introduced.

$$\begin{aligned} \omega &= \langle\omega\rangle \\ \omega_3 &= \langle\omega_3\rangle \pm \Delta\omega_3 \\ \omega_4 &= \langle\omega_4\rangle \pm \Delta\omega_4 \end{aligned} \tag{107}$$

In the $\langle L\rangle$-system, δ_ω is effectively invisible by operating the transverse Lorentz boost. $\Delta\omega_3$ and $\Delta\omega_4$ include not only $\delta\omega_3$ and $\delta\omega_4$ but also the energy uncertainties originating from absorbing $\delta\omega$ by transition from L-system to $\langle L\rangle$-system. The energy and the transverse momentum of the incident photons, ω and $p_{\rm T}$, have relations between L-system and $\langle L\rangle$-system as follows:

$$\begin{aligned}
\begin{pmatrix} \omega_1 \\ p_{1T} \end{pmatrix} &= \gamma \begin{pmatrix} 1 & -\beta \\ -\beta & 1 \end{pmatrix} \begin{pmatrix} \langle\omega\rangle \\ \langle\omega\rangle \sin\vartheta \end{pmatrix}, \\
\begin{pmatrix} \omega_2 \\ p_{2T} \end{pmatrix} &= \gamma \begin{pmatrix} 1 & -\beta \\ -\beta & 1 \end{pmatrix} \begin{pmatrix} \langle\omega\rangle \\ -\langle\omega\rangle \sin\vartheta \end{pmatrix},
\end{aligned} \tag{108}$$

where β is the relative velocity with respect to the velocity of light c and $\gamma = (1-\beta^2)^{-1/2}$. From Eq.(108), ω_1 and ω_2 are expressed as

$$\begin{aligned}
\omega_1 &= \gamma\langle\omega\rangle(1-\beta\sin\vartheta) \equiv \langle\omega\rangle - \delta\omega \equiv \langle\omega\rangle\,(1-\delta r)\,, \\
\omega_2 &= \gamma\langle\omega\rangle(1+\beta\sin\vartheta) \equiv \langle\omega\rangle + \delta\omega \equiv \langle\omega\rangle\,(1+\delta r)\,,
\end{aligned} \tag{109}$$

where $\delta r \equiv \delta\omega/\langle\omega\rangle$ is the relative line width with respect to the mean energy of the creation laser.

β for ω_1 and ω_2 satisfies the following equations with introducing the notation β_1 and β_2 correspond to ω_1 and ω_2, respectively with $\delta r \ll 1$.

$$\begin{aligned}
(1+\sin^2\vartheta - 2\delta r)\beta_1^2 - 2\sin\vartheta\beta_1 + 2\delta r = 0, \\
(1+\sin^2\vartheta + 2\delta r)\beta_2^2 + 2\sin\vartheta\beta_2 - 2\delta r = 0.
\end{aligned} \tag{110}$$

In the case of β_1, the following solution is given with $\vartheta \ll 1$.

$$\beta_{1\pm} \equiv \frac{\vartheta \pm \sqrt{D}}{1+\vartheta^2-2\delta r} \sim (1-\vartheta^2+2\delta r)\left(\vartheta \pm \sqrt{D}\right), \tag{111}$$

where

$$D \sim \vartheta^2 - (1+\vartheta^2-2\delta r)2\delta r \sim \vartheta^2 - 2\delta r. \tag{112}$$

The constraint of $D \geq 0$ gives

$$2\delta r \leq \vartheta^2. \tag{113}$$

If this is satisfied, $\sqrt{D} \sim (\vartheta^2-2\delta r)^{1/2} \sim \vartheta - \delta r/\vartheta$ with $\delta r \ll 1$ gives

$$\vartheta \pm \sqrt{D_1} \sim \vartheta \pm \left(\vartheta - \frac{\delta r}{\vartheta}\right). \tag{114}$$

As a result, $\beta_{1\pm}$ are expressed as

$$\begin{aligned}\beta_{1+} &\sim (1-\vartheta^2+2\delta r)\left(2\vartheta-\frac{\delta r}{\vartheta}\right)\sim 2\vartheta-\frac{\delta r}{\vartheta},\\ \beta_{1-} &\sim (1-\vartheta^2+2\delta r)\left(\frac{\delta r}{\vartheta}\right)\sim \frac{\delta r}{\vartheta}>0,\end{aligned} \tag{115}$$

where β_{1+} is not acceptable because the limit of $\delta r \to 0$ indicates $\beta = 0$.

β_2 is similarly obtained as

$$\begin{aligned}\beta_{2+} &\sim (1+\vartheta^2+2\delta r)\left(\frac{\delta r}{\vartheta}\right)\sim \frac{\delta r}{\vartheta}>0,\\ \beta_{2-} &\sim (1+\vartheta^2+2\delta r)\left(-2\vartheta-\frac{\delta r}{\vartheta}\right)\sim -2\vartheta-\frac{\delta r}{\vartheta},\end{aligned} \tag{116}$$

where β_{2-} is not acceptable because the limit of $\delta r \to 0$ indicates $\beta = 0$ as well as β_{1+}.

As a result, β is given as

$$\beta \sim \beta_{1-} = \beta_{2+} = \frac{\delta r}{\vartheta}. \tag{117}$$

By substituting δr in Eq.(117) into Eq.(113), the range of β is expressed as

$$\beta < \frac{\vartheta}{2}. \tag{118}$$

Among ϑ within $\Delta\vartheta$, ϑ_r is effectively enhanced based on the Breit-Wigner distribution in the averaging process of the square of the invariant scattering amplitude around $E_{\rm CMS} = 2\sin\vartheta_r\langle\omega\rangle$. Therefore, for a given mass $m \sim 2\langle\omega\rangle\vartheta_r$ with $\vartheta_r \ll 1$, the effective physical limit on β is expressed as

$$\beta_r \equiv \frac{\delta r}{\vartheta_r} < \frac{\vartheta_r}{2}. \tag{119}$$

On the other hand, the full line width of the creation laser $\Delta r \equiv \delta\omega_{\rm full}/\langle\omega\rangle$ is intrinsically determined. Therefore, the maximum range of β is given as

$$0 < \beta < \beta_c \equiv \frac{\Delta r}{\vartheta}. \tag{120}$$

If β_c is smaller than β_r, the upper limit of β_r is constrained as $\beta_r \le \beta_c$ duo to the instrumental limit of the spectrum width of the creation laser. Therefore smaller β, either β_c or β_r has to be chosen.

The range of u originating from the spectrum width of the creation laser in the $\langle L\rangle$-system is notated as $\underline{u}_c \leq u \leq \overline{u}_c$. $\underline{u}_c$ and $\overline{u}_c$ are evaluated as

$$\begin{aligned}
\overline{u}_c\langle\omega\rangle &\sim l_{i+}u\langle\omega\rangle\gamma(1+\beta\vartheta) \equiv l_{i-}u\langle\omega\rangle \min\{\gamma_c(1+\Delta r), \quad \gamma_r(1+\frac{1}{2}\vartheta_r^2)\} \\
\underline{u}_c\langle\omega\rangle &\sim l_i u\langle\omega\rangle\gamma(1-\beta\vartheta) \equiv l_i u\langle\omega\rangle \min\{\gamma_c(1-\Delta r), \quad \gamma_r(1-\frac{1}{2}\vartheta_r^2)\}
\end{aligned} \tag{121}$$

where l_i represents the process to choose a ω_4 within the relative line width of the inducing laser with $l_{i\pm} \equiv 1 \pm \delta\omega_4/\langle\omega_4\rangle$, γ_c and γ_i are defined as $\gamma_c = (1-\beta_c^2)^{-1/2}$ and $\gamma_r = (1-\beta_r^2)^{-1/2}$ respectively, and $\min\{A, B\}$ requires to choose smaller one between A and B.

The effective spectrum width of the inducing laser broadens by absorbing that of the creation laser in $\langle L\rangle$-system. We introduce a following notation as including the effect of the spectrum widths of the creation and the inducing lasers

$$\omega_{<4>} \equiv l_c l_i u\langle\omega\rangle, \tag{122}$$

where $l_c \equiv 1 \pm \delta u_c/u$ with $\delta u_c \equiv (\overline{u_c} - \underline{u_c})/2$. The inclusive uncertainty on ω_4 in the $\langle L\rangle$-system is evaluated as

$$\delta^2\omega_{<4>} = \left(\frac{\partial\omega_{<4>}}{\partial l_i}\right)^2 \delta^2 l_i + \left(\frac{\partial\omega_{<4>}}{\partial l_c}\right)^2 \delta^2 l_c = u^2\langle\omega\rangle^2 \left[\left(\frac{\delta u_4}{u}\right)^2 + \left(\frac{\delta u_c}{u}\right)^2\right]. \tag{123}$$

The inclusive uncertainty on u is given as

$$\delta u_{\rm inc} \equiv \frac{\delta\omega_{<4>}}{\langle\omega\rangle} = u\sqrt{\left(\frac{\delta u_4}{u}\right)^2 + \left(\frac{\delta u_c}{u}\right)^2}. \tag{124}$$

The upper and lower limits of u is obtained as

$$\begin{aligned}
\overline{u} &\equiv u + \delta u_{\rm inc}, \\
\underline{u} &\equiv u - \delta u_{\rm inc},
\end{aligned} \tag{125}$$

respectively.

Appendix D: Evaluation of the signal yield in QPS

The signal yield $\mathcal{Y}$ in QPS is evaluated as following policy.

$$\mathcal{Y} = \mathcal{D}[\mathrm{s/L^3}]\overline{\Sigma}[\mathrm{L^3/s}], \tag{126}$$

where $\mathcal{D}$ is the time-integrated density and Σ is the interaction volume per unit time.

From Eq.(2.5) of Ref.[39], the differential cross section per solid angle of the signal photon is expressed as

$$\frac{d\sigma}{d\Omega_3} = \left(\frac{1}{8\pi\omega}\right)^2 \sin\vartheta^{-4} \left(\frac{\omega_3}{2\omega}\right)^2 |\mathcal{M}_S(\vartheta)|^2. \tag{127}$$

The output angle of the signal photon θ_3 fluctuates by the effect of the spectrum width of the inducing laser $\delta\omega_4$. The integrated cross section over the range of θ_3 is expressed as

$$\sigma(\vartheta) = \frac{\mathcal{F}_S|\mathcal{M}_S(\vartheta)|^2}{(8\pi\omega)^2 \sin^4\vartheta} \int_{\underline{\theta_3}}^{\overline{\theta_3}} \left(\frac{\omega_3}{2\omega}\right)^2 \sin\theta_3 d\theta_3, \tag{128}$$

where $\overline{\theta_3}$ and $\underline{\theta_3}$ are the upper and lower limits of θ_3, respectively. The interaction cross section into the interaction volume per unit time $\Sigma(\vartheta)$ is denoted as

$$\Sigma(\vartheta) = K(\vartheta)\sigma(\vartheta) \sim \frac{2c^3\mathcal{F}_S|\mathcal{M}_S(\vartheta)|^2}{(8\pi)^2} \left(\frac{\lambda_c}{2\pi c}\right)^2 \frac{\delta u}{4} \quad \left[\mathrm{L^3/s}\right] \tag{129}$$

where $K(\vartheta)$ is the relative velocity of incoming particle beams defined as

$$K(\vartheta) \equiv \sqrt{(\vec{v_1} - \vec{v_2})^2 - \frac{(\vec{v_1} \times \vec{v_2})^2}{c^2}} = 2c\sin^2\vartheta, \tag{130}$$

λ_c is the wavelength of the creation laser, $\delta u \equiv \overline{u} - \underline{u}$. The averaged value of $\Sigma(\vartheta)$ over ϑ is expressed as

$$\begin{aligned}\overline{\Sigma} &= \int_0^{\pi/2} d\vartheta \rho(\vartheta)\Sigma(\vartheta) \\ &= \frac{c\mathcal{F}_S\lambda_c^2\delta u}{2(16\pi^2)^2}\int_0^{\pi/2} d\vartheta\rho(\vartheta)|\mathcal{M}_S(\vartheta)|^2 \\ &\sim \frac{c\mathcal{W}\mathcal{F}_S\lambda_c^2\delta u}{4\sqrt{\pi}(4\pi)^3}\left(\frac{\vartheta_r}{\Delta\theta}\right)\left(\frac{gm}{M}\right)^2. \end{aligned} \tag{131}$$

Then, we evaluate the time-integrated density factor $\mathcal{D}$ based on the Gaussian laser beam propagation. The density profile of an incident Gaussian laser at the focal point $z = 0$ with the pulse duration time τ_c propagating over the focal length f along z-axis is expressed as

$$\rho_c(x,y,z,t) = \frac{2N_c}{\pi w^2(z)}\exp\left\{-2\frac{x^2+y^2}{w^2(z)}\right\}\frac{1}{\sqrt{\pi}c\tau_c}\exp\left\{-\left(\frac{z^{'}}{c\tau_c}\right)^2\right\}, \tag{132}$$

where N_c is the number of creation photons per pulse.

The time-integrated density factor for the creation laser $\mathcal{D}_c$ is expressed as

$$\begin{aligned}\mathcal{D}_c &= \int_{-f/c}^{0} dt\int_{-\infty}^{\infty} dx\int_{-\infty}^{\infty} dy\int_{-\infty}^{\infty} dz{\rho_c}^2(x,y,z,t) \\ &= \frac{N_c^2}{\sqrt{2\pi}}\frac{1}{\pi{w_0}^2}\frac{1}{c\tau_c}\frac{z_R}{c}\tan^{-1}\left(\frac{f}{z_R}\right) \quad \left[s/L^3\right], \end{aligned} \tag{133}$$

where the time integration is performed during the pulse propagation from $z = -f$ to $z = 0$, since the photon-photon scattering never occurs after they pass through the focal point.

The effects of the inducing laser beam under the practical experimental condition are should be considered. The inducing effect is expected only when the momentum of the one of the final state photon p_4 coincides with a photon momentum included in the coherent state of the inducing beam. When the final state of photons accept the inducing effect, it should satisfies following resonance condition,

$$E_{\rm CMS} = m = 2\omega\sin\vartheta_r. \tag{134}$$

Therefore, p_4 has to be expressed with the condition $\vartheta = \vartheta_r$. Then, following relations are obtained with approximation $\vartheta_r \ll 1$,

$$\theta_4 \sim \mathcal{R}^{-1/2}\vartheta_r \quad \text{and} \quad \theta_3 \sim \mathcal{R}^{1/2}\vartheta_r, \tag{135}$$

where

$$\mathcal{R} \equiv \frac{\sin\theta_3}{\sin\theta_4} = \frac{\omega_4}{\omega_3} = \frac{u}{2-u}. \tag{136}$$

These relations indicate that the final state photons emitted as a ring-like patterns.

Next, the overlapping between the p_4 and the fraction of photon momenta in the inducing beam is discussed. The electric field distribution at $z = 0$ is described as following expression,

$$\begin{aligned} \vec{E}(k_x, k_y; z=0) &= \vec{E_0}\frac{w_0^2}{4\pi}\exp\left\{-\frac{w_0^2}{4}(k_x^2+k_y^2)\right\} \\ &\equiv \vec{E_0}\frac{w_0^2}{4\pi}\exp\left\{-\frac{w_0^2}{4}k_T^2\right\}, \end{aligned} \tag{137}$$

where the transverse wave vector component $k_T^2 = k_x^2 + k_y^2$ is introduced.

The electric filed distribution of the inducing beam is expressed as

$$\vec{E_4}(k_x, k_y; z=0) = \vec{E_{04}}\frac{w_{04}^2}{4\pi}\exp\left\{-\frac{w_{04}^2}{4}(k_{T4}^2)\right\} \tag{138}$$

The acceptance factor $\mathcal{A}_i$ is evaluated as

$$\begin{aligned} \mathcal{A}_i &\equiv \frac{\int_{\underline{k_{T4}}}^{\overline{k_{T4}}} 2\pi k_{T4}E_4^2 dk_{T4}}{\int_0^\infty 2\pi k_{T4}E_4^2 dk_{T4}} = e^{-\frac{w_{04}^2}{2}\underline{k_{T4}}^2} - e^{-\frac{w_{04}^2}{2}\overline{k_{T4}}^2} \\ &\sim \frac{w_{04}^2}{2}(\overline{k_{T4}}^2 - \underline{k_{T4}}^2) \sim \frac{w_{04}^2 k_4^2}{2}\vartheta_r^2(\underline{\mathcal{R}}^{-1} - \overline{\mathcal{R}}^{-1}) \\ &\sim 2(\underline{\mathcal{R}}^{-1} - \overline{\mathcal{R}}^{-1})\left(\frac{\vartheta_r}{\Delta\theta}\right)^2 = 4\frac{\overline{u}-\underline{u}}{\overline{u}\underline{u}}\left(\frac{\vartheta_r}{\Delta\theta}\right)^2, \end{aligned} \tag{139}$$

with

$$k_{T4} \equiv k_4 \sin\theta_4 \sim k_4 \mathcal{R}^{-1/2}\vartheta_r, \tag{140}$$

where $\underline{k_{T4}}$ and $\overline{k_{T4}}$ defined as the lower and upper values of k_{T4}, the approximation $w_{04}k_{T4} \ll 1$ and $k_{T4} \sim k_4\mathcal{R}^{-1/2}\vartheta_r$ are applied in the first and second lines, respectively, and

$$w_{04}k_4 = \frac{2\pi w_{04}}{\lambda_i} \equiv \frac{2}{\Delta\theta_4} \sim \frac{2}{\Delta\theta} \tag{141}$$

is substituted in the third line.

Furthermore, the overlapping effect of pulse durations of the creation and inducing lasers should be considered. This is because the inducing photons contribute the enhancement effect have to coincide with the creation photons at the time-dimension. When we simulate the pulse duration of the creation laser τ_c is shorter that that of the inducing laser τ_i, the entire inducing effect is expressed as

$$\mathcal{I} = \mathcal{A}_i \left(\frac{\tau_c}{\tau_i}\right) N_i = 4\frac{\overline{u}-\underline{u}}{\overline{u}\underline{u}} \left(\frac{\vartheta_r}{\Delta\theta}\right)^2 \left(\frac{\tau_c}{\tau_i}\right) N_i. \tag{142}$$

The density factor including the inducing laser effect $\mathcal{D}_{c+i}$ is expressed as follows:

$$\begin{aligned}
\mathcal{D}_{c+i} &= C_{\rm mb}\mathcal{D}_c\mathcal{I} \\
&= C_{\rm mb}\frac{N_c^2}{\sqrt{2\pi}}\frac{1}{\pi {w_0}^2}\frac{1}{c\tau_c}\frac{z_R}{c}\tan^{-1}\left(\frac{f}{z_R}\right) 4\delta\mathcal{U}\left(\frac{\vartheta_r}{\Delta\theta}\right)^2\left(\frac{\tau_c}{\tau_i}\right) N_i \\
&= \frac{4}{\sqrt{2\pi}}\frac{1}{c^2\lambda_c\tau_c}\left(\frac{\tau_c}{\tau_i}\right)\tan^{-1}\left(\frac{\pi d^2}{4\ f\lambda_c}\right)\left(\frac{\vartheta_r}{\Delta\theta}\right)^2 \\
&\times \frac{\overline{u}-\underline{u}}{\overline{u}\underline{u}} C_{\rm mb}N_c^2N_i,
\end{aligned} \tag{143}$$

where $C_{\rm mb} = 1/2$ is the combinatorial factor originating from the combination of choosing two photons among frequency multimode states in creation and inducing lasers.

The signal yield $\mathcal{Y}$ is finally expressed as

$$\begin{aligned}
\mathcal{Y} &= \mathcal{D}_{c+i}\overline{\Sigma} \\
&= \frac{4}{\sqrt{2\pi}}\frac{1}{c^2\lambda_c\tau_c}\left(\frac{\tau_c}{\tau_i}\right)\tan^{-1}\left(\frac{\pi d^2}{4\ f\lambda_c}\right)\left(\frac{\vartheta_r}{\Delta\theta}\right)^2\frac{\overline{u}-\underline{u}}{\overline{u}\underline{u}} C_{\rm mb}N_c^2N_i \\
&\times \frac{c\mathcal{W}\mathcal{F}_S\lambda_c^2\delta u}{4\sqrt{\pi}(4\pi)^3}\left(\frac{\vartheta_r}{\Delta\theta}\right)\left(\frac{gm}{M}\right)^2 \\
&\sim \frac{1}{64\sqrt{2}\pi^4}\left(\frac{\lambda_c}{c\tau_c}\right)\left(\frac{\tau_c}{\tau_i}\right)\left(\frac{f}{d}\right)^3\tan^{-1}\left(\frac{\pi d^2}{4\ f\lambda_c}\right) \\
&\times \frac{(\overline{u}-\underline{u})^2}{\overline{u}\underline{u}}\left(\frac{gm[eV]}{M[eV]}\right)^2\left(\frac{m[eV]}{\omega[eV]}\right)^3\mathcal{W}\mathcal{F}_S C_{\rm mb}N_c^2N_i,
\end{aligned} \tag{144}$$

where the parameters specified with [eV] apply natural units.

Appendix E: Scalar-tensor theory and dilaton

Here physics backgrounds for the scalar-tensor theory and dilaton fields are introduced by referring to Ref.[13]. The accelerating universe was discovered by observations of redshifts of type Ia supernova. It is supposed that unknown energy called dark energy expands the universe. In modern cosmology, the cosmological constant Λ is interpreted as the origin of dark energy.

The cosmological constant Λ is appeared in the Einstein field equations as follows:

$$R_{\mu\nu} - \frac{1}{2}Rg_{\mu\nu} + \Lambda g_{\mu\nu} = \frac{8\pi}{c^4}GT_{\mu\nu}, \tag{145}$$

where $R_{\mu\nu}$ is the Ricci tensor, R is the scalar curvature, $g_{\mu\nu}$ is the metric tensor, G is the gravitational constant, and $T_{\mu\nu}$ is the stress-energy tensor. If we assume the cosmological constant Λ as the vacuum energy, the theoretical value of Λ is estimated as $\Lambda_{\rm vac} \sim M_P^4 \sim 1$ with Planck units $c = \hbar = M_P = 1$, where Planck mass $M_P = \sqrt{\frac{\hbar c}{8\pi G}} = 2.43 \times 10^{18}$ GeV. On the other hand, the observation value of Λ is given as $\Lambda_{\rm obs} \sim 10^{-120}$. This unreasonable deviation is called "cosmological constant problem".

Scalar-tensor theory is the alternative gravitational theory which can solve the cosmological constant problem. Scalar-tensor theory is propounded by P.Jordan in 1955 to discuss about the time variability of the gravitational constant G. The first motivation is come from considering why gravitational force is so weak compared to other forces. The time variability of G is obtained by introducing scalar field ϕ.

The Lagrangian is expressed as follows:

$$\mathcal{L} = \sqrt{-g}\left(\frac{1}{2}\xi\phi^2 R - \frac{1}{2}\epsilon g^{\mu\nu}\partial_\mu\phi\partial_\nu\phi + L_{\rm matter} - \Lambda\right), \tag{146}$$

where ξ is the dimensionless constant, $\epsilon = \pm 1$, $L_{\rm matter}$ is the matter field Lagrangian. The time variability of G is expressed as $\xi\phi^2 = (8\pi G_{\rm eff})^{-1}$. However, the scale factor of universe $a(t) = $ const is given from Eq.(147). This means the universe is static, which is not consistent with the observations of the expanding universe.

The physical frame which has the invariable G is obtained from the con-

formal transformation of Eq.(147). The transformation satisfies

$$g_{*\mu\nu} = \Omega^2 g_{\mu\nu}, \tag{147}$$

where

$$\Omega^2 = \xi\phi^2, \tag{148}$$

$$\phi = \xi^{-1/2} \exp(\zeta\sigma), \tag{149}$$

with $\zeta^{-2} = 6 + \epsilon\xi^{-1}$. Then Eq.(147) is converted as

$$\mathcal{L} = \sqrt{-g_*}\left(\frac{1}{2}R_* - \frac{1}{2}g_*^{\mu\nu}\partial_\mu\sigma\partial_\nu\sigma + L_{*matter} - \Lambda\exp(-4\zeta\sigma)\right). \tag{150}$$

The transformed conformal frame is named "Einstein frame". The invariable G is expressed in the first term of right side. The Einstein frame has the highly important aspects that

$$a = t^{1/2}, \tag{151}$$

$$\rho_\sigma = \frac{1}{2}\left(\frac{d\sigma}{dt}\right)^2 + \Lambda\exp(-4\zeta\sigma) = \frac{3}{16}\zeta^{-2}t_*^{-2}, \tag{152}$$

where a is the scale factor of the universe and ρ_σ is the energy density of the scalar field σ. The expansion of the universe is expressed in Eq.(151) and the time dependence of it is consistent with the expected result.

Equation (152) gives t^{-2} dependence of $\Lambda_{\rm obs}$. Now we go back to the cosmological constant problem. The age of universe $t_0 = 1.37 \times 10^{10}$ years is expressed as $t_0 \sim 10^{60}$ with Planck units. On the other hand, $\Lambda_{\rm obs} \propto t^{-2}$ is obtained from Eq.(152). As a result,

$$\Lambda_{\rm obs} = \Lambda_{\rm vac}t_0^{-2} = \Lambda_{\rm vac} \times 10^{-120} \tag{153}$$

is derived. Thus, the descriptions of the Einstein frame can be the solution of the cosmological constant problem.

The Einstein frame seems to be having good agreement with our realistic universe. However, the Einstein frame has the crucial problem that the mass of particles m has the time variability. This property is come from $L_{\rm matter}$ in Eq.(147). Here $L_{\rm matter}$ is expressed as

$$L_{\rm matter} = \sqrt{-g}\left(-\frac{1}{2}g^{\mu\nu}\partial_\mu\psi\partial_\nu\psi - \frac{1}{2}m^2\psi^2\right), \tag{154}$$

where ψ is the neutral scalar field. In the Einstein frame $L_{*\rm matter}$ is expressed as

$$L_{*\rm matter} = \sqrt{-g_*}\left(-\frac{1}{2}g_*^{\mu\nu}\partial_\mu\psi_*\partial_\nu\psi_* - \frac{1}{2}m_*^2\psi_*^2\right), \tag{155}$$

where m_* has the time dependence with $m_* \propto t_*^{-1/2}$.

To introduce the constant mass to the Einstein frame, the second term of the right side in Eq.(154) is modified as

$$L_{\phi\psi} = -\frac{1}{2}\sqrt{-g}h^2\phi^2\psi^2, \tag{156}$$

where h is the dimensionless coupling constant. In the Einstein frame, Eq. (157) is expressed as

$$L_{\phi\psi} = -\frac{1}{2}\sqrt{-g_*}m_\sharp^2\psi_*^2, \tag{157}$$

where $m_\sharp^2 = h^2\xi^{-1}$= const. The Einstein frame, finally, has consistency with our realistic universe.

Our nature has chosen the Einstein frame as the specific conformal frame in spite of the nature has the degree of freedom of what frame choose. It is interpreted as the spontaneous breaking of the conformal symmetry. From Eq.(149), σ is regarded as the Nambu-Goldstone field called dilaton.

Dilaton has a nonzero mass duo to the self-energy. The mass of dilaton m_σ is given by [39]

$$m_\sigma^2 \sim \frac{m_q^2 M_{\rm ssb}^2}{M_P^2} \sim (10^{-9}\ {\rm eV})^2, \tag{158}$$

where m_q is a typical mass of the light quarks $\sim$ MeV, $M_{\rm ssb} \sim$ TeV is the effective cutoff of the self-energy of dilaton relevant to the mass scale of the supersymmetry-braking. This calculation is based on the one-loop diagram of the light quarks and leptons couple to dilaton. When the two-loop diagram of the σ - Higgs coupling is taken into the account, $m_\sigma \sim$ sub-μeV is obtained.

The coupling constant for the σ - photon coupling is expressed as [39]

$$\frac{g}{M} = \frac{(2\alpha/3\pi)\mathcal{Z}\xi}{M_P}, \tag{159}$$

where $\mathcal{Z} = 5$ is the effective number of the fundamental charged particles (the light quarks and leptons) in the loop, and ξ is a constant of the order unity. The magnitude of the coupling constant is roughly estimated to $g/M \sim 10^{-20}$ eV $\sim G^{1/2}$.

Appendix F: Axion theory

Axion is the pseudoscalar NG boson as a result of the breaking of the Peccei-Quinn (PQ) symmetry. Theoretical backgrounds of axion are introduced in this section by referring to [54].

The PQ symmetry is the chiral symmetry introduced to solve the strong CP problem. The QCD Lagrangian has the term violates the CP invariance as [55]

$$L_\theta = \theta \frac{g_s^2}{32\pi^2} F_a^{\mu\nu} \tilde{F}_{a\mu\nu}, \tag{160}$$

where θ is the phase parameter relevant to the chiral transformation, g_s is the coupling constant of the QCD, $F_a^{\mu\nu}$ is the strength of the gluon field, and $\tilde{F}_{a\mu\nu}$ is its dual. θ has a degree of freedom corresponds to the chiral transition, however, its experimental value is constrained to $\theta_{\rm obs} < 10^{-9}$ by the measurements of the electric dipole moment of neutron. Why is θ_{obs} so small is known as the strong CP problem.

To solve the strong CP problem, a global chiral symmetry $U(1)_{\rm PQ}$ is introduced. As a result, Eq.(160) substitute for

$$L_\theta = \left(\theta + \frac{a}{v}N\right) \frac{g_s^2}{32\pi^2} F_a^{\mu\nu} \tilde{F}_{a\mu\nu}, \tag{161}$$

where a indicates the axion field, v is the vacuum expectation value of the Higgs field, and N is the model-dependent factor. a takes the following form.

$$a = \langle a \rangle + a_{\rm phys}, \tag{162}$$

where $\langle a \rangle$ is given by the minimum value of the potential of a, and $a_{\rm phys}$ indicates the excitation of the potential. Therefore, $a_{\rm phys}$ represents the observable axion.

When the PQ symmetry breaks spontaneously to satisfy

$$\left(\theta + \frac{\langle a \rangle}{v}N\right) = 0, \tag{163}$$

the strong CP problem can be solved and axion appears as the NB boson.

The interaction Lagrangian coupling between two photons and axion introduced in Eq.(14) is given again.

$$-L_\sigma = gM^{-1}\frac{1}{4} F_{\mu\nu}\tilde{F}^{\mu\nu}\sigma. \tag{164}$$

The original PQ model predicts that axion may also couple to the charged particles directly and the mass scale of the PQ symmetry braking takes

$M \sim (\sqrt{2}G_F)^{-1/2} \equiv v_F$, where G_F is the coupling constant of the weak interactions. However, this prediction is excluded by the previous axion search experiments, for example, $K^+ \to \pi + a$ search at KEK [56] and $J/\psi \to \gamma + a$ search at SLAC [57], where a represents axion.

From the previous experimental results, a "invisible axion" model with $M \gg v_F$ has been advocated. Here the typical invisible axion model called the "KSVZ model" [36, 37] is introduced. The KSVZ model predicts that a scalar field σ with $M_\sigma \gg v_F$ carries PQ charge and a superheavy quark Q plays a role as the only field carries PQ charge with $M_Q \sim M_\sigma$. As a result, axion does not interact with leptons and it only interacts with the light quarks via the strong and electromagnetic anomalies [55].

In the invisible axion model, the mass of axion is given as

$$m_\sigma = \frac{m_\pi F_\pi}{M_\sigma}\frac{\sqrt{z}}{1+z} = 0.62 \text{ eV}\left(\frac{10^7 \text{ GeV}}{\text{M}_\sigma}\right), \tag{165}$$

where $m_\pi = 135$ MeV is the mass of π_0, $F_\pi = 93$ MeV is the decay constant of π_0, $z = \frac{m_u}{m_d} = 0.568 \pm 0.042$ with the masses of up quark and down quark, m_u and m_d, respectively.

The coupling constant for the axion - photon coupling is expressed as

$$\frac{g}{M} = \frac{e^2}{8\pi^2 M_\sigma}\left(\frac{E}{N} - 1.92\right), \tag{166}$$

with

$$\begin{aligned} N &= \sum_j Q_5(PQ)_j, \\ E &= 2\sum_j Q_5(PQ)_j Q_j^2 N_{cj}, \end{aligned} \tag{167}$$

where $Q_5(PQ)_j$ is the PQ charge of the fermions, Q_j is the electromagnetic charge in unit of e, and N_{cj} is the color degree of freedom. Thus the values of N and E are the model-dependent because the number of species carry the PQ charge depends on the model.

References

[1] Y.Numbu, Phys. Rev. Lett **4**, 380 (1960).

[2] J.Goldstone, Nuevo Cim. **19**, 154 (1961).

[3] B.Schmidt et al., Astrophys.J **507**, 46 (1998).

[4] A.G.Riess et al., Astron.J **116**, 1009 (1998).

[5] S.Perlmutter et al., Astrophys.J **517**, 565 (1999).

[6] Y. Fujii and K. Maeda, *The Scalar-Tensor Theory of Gravitation*, Cambridge Univ. Press (2003).

[7] Y.Fujii, arxiv:1502.1360 [gr-qc] (2015)

[8] S. J. Smullin et al., Phys. Rev. D **72**, 122001 (2005); **72**, 129901 (2005) [erratum].

[9] S. K. Lamoreaux, Phys. Rev. Lett. **78**, 5 (1997); **81**, 5475 (1998) [erratum].

[10] M. Bordag et al., Phys. Rev. D. **58**, 075003 (1998); **81**, 5475 (1998) [erratum].

[11] J. Chiaverini et al., Phys. Rev. Lett. **90**, 151101 (2003).

[12] J.C.Long et al., Nature **421**, 922 (2003).

[13] D.B.Kaplan and M.B.Wise, J.High Energy Phys. **07**, 037 (2000).

[14] N.A.Hamed, S.Dimopoulos, and G.Dvali. Phys. Rev. D **59**, 086004 (1999).

[15] S. Weinberg, Phys. Rev. Lett **40**, 223 (1978).

[16] F. Wilczek, Phys. Rev. Lett **40**, 271 (1978).

[17] M. P. Hertzberg, M. Tegmark, and F. Wilczek, Phys. Rev. D **78**, 083507 (2008).

[18] O. Wantz and E. P. S. Shellard, Phys. Rev. D **82**, 123508 (2010).

[19] J.H.Smith, E.M.Purcell, and N.F.Ramsey. Phys.Rev. **108**, 120 (1957).

[20] R. D. Peccei and H. R. Quinn, Phys. Rev. Lett **38**, 1440 (1977).

[21] S. Moriyama et al., Phys. Lett. B **434**, 147 (1998).

[22] Y. Inoue et al., Phys. Lett. B **536**, 18 (2002).

[23] Y. Inoue et al., Phys. Lett. B **668**, 93 (2008).

[24] K. Zioutas et al. (CAST Collaboration), Phys. Rev. Lett. **94**, 121301 (2005).

[25] S. Andriamonje et al. (CAST Collaboration), J. Cosmol. Astropart. Phys. **04**, 010 (2007).

[26] E. Arik et al. (CAST Collaboration), J. Cosmol. Astropart. Phys. **02**, 008 (2009).

[27] M. Arik et al. (CAST Collaboration), Phys. Rev. Lett. **107**, 261302 (2011).

[28] R. Cameron et al. (BRFT Collab.), Phys. Lett. D **57**, 3873 (1993).

[29] E. Zavattini et al. (PVLAS Collab.), Phys. Lett. D **77**, 032006 (2008).

[30] F. D. Valle et al. (PVLAS Collab.), Phys. Lett. D **90**, 092003 (2014).

[31] P. Pugnat et al. (OSQAR Collab.), Phys. Lett. D **78**, 092003 (2008).

[32] K. Ehret et al. (ALPS Collab.), Phys. Lett. B **689**, 149 (2010).

[33] S.J.Asztalos et al. (ADMX Collab.), Phys. Rev. D **69**, 01101 (2004).

[34] S.J.Asztalos et al. (ADMX Collab.), Phys. Rev. Lett. **104**, 041301 (2010).

[35] I.G.Irastorza et al., JCAP **06**, 013 (2011).

[36] J. E. Kim, Phys. Rev. Lett. **43**, 103 (1979).

[37] M. A. Shifman, A. I. Vainshtein and V. I. Zakharov, Nucl. Phys. B **166**, 493 (1980).

[38] J. F. Reintjes, *Nonlinear Optical Parametric Processes in Liquids and Gases*, ACADEMIC PRESS, INC. (1984).

[39] Y. Fujii and K. Homma, Prog. Theor. Phys **126**, 531 (2011); Y. Fujii and K. Homma, Prog. Theor. Exp. Phys. (2014) 089203.

[40] K. Homma, Prog. Theor. Exp. Phys. (2012) 04D004; K. Homma, Prog. Theor. Exp. Phys. (2014) 089201.

[41] S. A. J. Druet and J.-P. E. Taran, Prog. Quant. Electr. **7**, 1 (1981).

[42] Amnon Yariv, *Optical Electronics in Modern Communications* Oxford University Press (1997).

[43] F. Moulin and D. Bernard, Opt. Commun. **164**, 137 (1999).

[44] E. Lundström et al., Phys. Rev. Lett. **96**, 083602 (2006).

[45] J. Lundin et al., Phys. Rev. A **74**, 043821 (2006).

[46] D. Bernard et al., Eur. Phys. J. D **10**, 141 (2000).

[47] T.Hasebe et al., Prog. Theor. Exp. Phys. 073C01 (2015).

[48] K. Homma, T. Hasebe, and K.Kume, Prog. Theor. Exp. Phys. 083C01 (2014).

[49] Y. Su et al., Phys. Rev. D **50**, 3614 (1994); **51**, 3135 (1995) [erratum].

[50] E. G. Adelberger et al., Phys. Rev. Lett. **98**, 131104 (2007);

[51] D. J. Kapner et al., Phys. Rev. Lett. **98**, 021101 (2007).

[52] ELI-NP web site; http://www.eli-np.ro.

[53] IZEST web site; http://www.izest.polytechnique.edu/jsp/accueil.jsp.

[54] 長島　順清, 高エネルギー物理学の発展, 朝倉書店 (1999).

[55] R. D. Peccei, Lect. Notes Phys. **741**, 3 (2008).

[56] Y. Asano et al., Phys. Lett. B. **107**, 159 (1981).

[57] C. Edwards et al., Phys. Rev. Lett. **48**, 903 (1982).

公表論文

(1) Search for sub-eV scalar and pseudoscalar resonances via four-wave mixing with a laser collider

Takashi Hasebe, Kensuke Homma, Yoshihide Nakamiya, Kayo Matsuura, Kazuto Otani, Masaki Hashida, Shunsuke Inoue, and Shuji Sakabe

Progress of Theoretical and Experimental Physics 073C01 (2015)

参考論文

(1) The first search for sub-eV scalar fields
via four-wave mixing at a quasi-parallel laser collider

Kensuke Homma, Takashi Hasebe, and Kazuki Kume

Progress of Theoretical and Experimental Physics
083C01 (2014)

(2) 真空内四光波混合光による sub-eV 中性ボゾンの
共鳴探索

本間謙輔, 長谷部孝, 久米一輝, 阪部周二, 橋田昌樹

高エネルギーニュース, vol32, No3, (2013) 171 - 177